AN ABSTRACT OF THE THESIS OF

Soon-Chang Yoon for the degree of Doctor of Philosophy in Atmospheric Sciences presented on March 15, 1983.

Title: The Structure of Turbulent Entraining Flow in an Annulus with a Rotating Screen

Redacted for Privacy

Abtract approved: _____
James W. Deardorff

Experiments on mixed-layer growth in an annulus with rotating screen are analyzed. Horizontal and vertical profiles of the mean velocities and turbulent intensities are obtained from velocity measurements with a hot-film anemometer. When the rotating screen covers the entire horizontal area, as in conventional annulus experiments, it was found that a turbulent Ekman layer of thickness two tenths of the typical mixed-layer depth exists just below the rotating screen; its termination prohibits the downward transport of the externally applied surface stress to the rest of the mixed layer. The measured turbulent intensities in a narrow region near the outer wall are an order of magnitude greater than those in the central region. A large secondary circulation is found to be important to the momentum transfer in the mixed layer.

The mean flow is found to be stable inertially in most of the annulus area except in the narrow region near the outer wall. Consequently, the entrainment occurs mostly by outer-wall turbulence, partially by the turbulence which is generated by the mean velocity shear across the entraining interface, and partially by outer-wall turbulence advected toward the inner wall by the secondary circulation. Therefore, the surface stress is not the proper parameter with which to scale the turbulence associated with the entrainment process. This indicates that the annulus experiments with the conventional screen-drive mode do not properly simulate the geophysical situation in which the the surface stress is the source of the turbulence in the mixed layer.

An effort has been made to make the rotating-screen annulus experiment relevant to geophysical situations. The screen is modified to occupy the inner 1/4 of the annulus area, and roughness elements are attached underneath the inner half of this screen. Then, the inertially stable region is found to be confined to a much smaller region near the inner wall, and the turbulence in the mixed layer to be relatively homogeneous. Consequently, the entrainment occurs more uniformly across the horizontal area. In these respects, it is concluded that the modified screen-drive mode is superior to the conventional screen-drive mode as a rotating-screen

annulus experiment for simulating geophysical flows.

The Structure of Turbulent Entraining Flow in an Annulus with a Rotating Screen

by

Soon-Chang Yoon

A THESIS

submitted to

Oregon State University

in partial fulfillment of
the requirements for the
degree of

Doctor of Philosophy

Completed March 15, 1983

Commencement June 1983

APPROVED:

Redacted for Privacy

Professor of Atmospheric Sciences in charge of major

Redacted for Privacy

Chairman of department of Atmospheric Sciences

Redacted for Privacy

Dean of Graduate School

Date thesis is presented March 15, 1983

Typed by researcher for Soon-Chang Yoon

ACKNOWLEDGMENT

I am deeply indebted to Professors James W. Deardorff and Glen E. Willis for their guidance and support throughout the course of my thesis work. Gratitude is also due to Professor W. Lawrence Gates, Chairman of the Department of Atmospheric Sciences, and all the staff members of the department for the great opportunity and helpful assistance they provided during my graduate education at OSU. I would also like to express my sincere thanks to Dr. Paul C. Katen for his generosities to allow me to use the computer facilities at his laboratory. I appreciate the offering of Mr. John Hubbe for reading the manuscript and suggesting better expressions in English. The technical expertise of Mr. Paul Stockton in all phases of the experimental work was indispensible.

Special gratitude is also owed to my friends, Yong-Joong Kang, Yong-Kuk Lee and Joo-Sik Shin. Their willingness to help me when I needed it was greatly appeciated. Finally, I want to express my sincere thanks to my parent and sister for their support throughout the course of this work. This research was supported by the National Science Foundation, Division of Atmospheric Sciences, under grant ATM 80-19778.

TABLE OF CONTENTS

LIST OF FIGURES

Fig. IV.20 Log-log plot of the entrainment rate versus the overall Richardson number in comparison with KPA's and SL's data

LIST OF TABLES

THE STRUCTURE OF TURBULENT ENTRAINING FLOW IN AN ANNULUS WITH A ROTATING SCREEN

I. INTRODUCTION

The atmospheric boundary layer is by definition turbulent, and is distinguished from the upper non-turbulent layer by its much greater mixing capability. The height of the boundary layer, h, varies from a few tens of meters on clear nights with light winds to one or two kilometers on sunny summer afternoons. Air pollutants emitted from a stack may affect the air quality in the boundary layer where we live unless the stack is higher than h at the time of emission, and the air quality will be worse when h is smaller. The boundary layer is also important to cloud modeling, since low-level convective clouds cannot form unless h reaches the local lifting-condensation level, and these clouds cannot develop vertically if the capping inversion atop the boundary layer is strong.

The height of the atmospheric mixed layer is important not only to these applications but also to many respects of atmospheric boundary-layer research. The mixed-layer height is a length scale that needs to be

known in order to nondimensionalize turbulence properties, and more importantly to determine the nondimensional parameters on which the transfer coefficients depend. The upper ocean is similarly turbulent, and the depth of its mixed layer varies from a few meters on a calm day to several tens of meters under an ocean storm condition. This depth is needed in order to predict the sea-surface temperature which is in turn important to the evolution of weather systems.

The mixed layer grows by entraining non-turbulent fluid into the turbulent fluid through the conversion of turbulent kinetic energy to potential energy. The entrainment rate, dh/dt, depends primarily on the buoyancy jump $\Delta b = \Delta\rho g/\rho$ and the turbulence or turbulent-momentum flux $\overline{v'w'}$ at the entraining interface. There, buoyancy forces destroy turbulence by the gravitational stability, so the entrainment rate decreases with an increase in the buoyancy jump. Sources of turbulence in the mixed layer are: mean-velocity shear $d\bar{v}/dz$ at the density interface, surface stress $\overline{v'w'}$ generated by surface wind, and destabilizing surface heat flux $\overline{T'w'}$ (or buoyancy flux $\overline{b'w'}$). Growth dynamics of the mixed layer are presented, for example, by Mahrt and Lenschow (1976) and Zeman and Tennekes (1977) for atmospheric applications. The dynamics of the ocean mixed layer is described by Niiler

(1975). In both atmospheric and oceanic cases their work depends on the results of laboratory experiments.

Traditionally, laboratory experiments have played essential roles in providing needed information for geophysical applications. Laboratory experiments on the mixed-layer growth by surface-heat flux were successfully performed in a convection tank by Willis and Deardorff (1974). Laboratory experiments simulating the mixed-layer growth by the surface stress generated from surface winds were initiated in an annulus with rotating screen by Kato and Phillips (1969), and later by Kantha, Phillips and Azad (1977). Their results have been believed to reflect one-dimensional entrainment processes in stratified flows of large horizontal extent such as the mixed-layer deepening in the upper ocean (Denman and Miyake, 1973). Effects of flow curvature within the annulus were neglected, and the circumferential (or tangential) flow component was likened to the downwind flow component within a rectilinear geophysical flow. However, recent measurement of a two-layer system (upper layer turbulent and denser lower layer non-turbulent) within an annulus by Scranton and Lindberg (1982) and by Jones and Mulhearn (1982) have indicated that the entrainment-rate data are strongly influenced by mean flow curvature and are therefore apparatus-dependent. Scranton and Lindberg

(1982) found that the momentum and turbulent kinetic energy of the flow in an annulus are non-homogeneous and radially stratified and that the secondary circulation motions are present and cannot be neglected. From these findings they concluded that the entrainment process is not one dimensional in an annulus experiment.

This conclusion was qualitatively verified from visual examination of the mixed-layer interface within the recently constructed annulus of Deardorff and Willis at the Oregon State University. The interface between the upper turbulent layer and the lower non-turbulent denser layer was seen to be very agitated near the outer wall of the annulus, and remarkably free of expected disturbances and entrainment cusps within the inner 50 - 85% of the annulus area. It was suggested by Deardorff (1981) that inertial stability was responsible for the problem over the bulk of the annulus where angular momentum increases outwards, with inertial instability perhaps occurring close to the outer wall. He suggested that the annulus screen drive might be modified so that the mean flow is more nearly one of constant angular momentum (irrotational) instead of nearly solid rotation.

This modification was made by altering the rotating screen so that it occupies only the inner 1/4 of the

annulus surface area (hereinafter referred to as 'inner-screen mode') and by adding roughness elements to the inner half of its underside to force any region of inertial stability near the inner wall to be confined to a smaller area. In this study we then sought to quantify the degree to which inertial stability and other curvature effects had been effectively removed without introducing excessive inertial instability. These results will be compared to the case of the conventional annulus where the rotating screen covers the entire annulus area (hereinafter referred to as 'full-screen mode') and the mean flow is close to solid rotation.

In the present work radial and vertical profiles of mean velocities and turbulent intensities were measured using a V-configuration hot-film anemometer. The measurements were analyzed in order to better understand complications introduced by the conventional screen drive (full-screen mode) and to demonstrate the improvements to the flow which can be made using the modified screen drive (inner-screen mode).

II. EXPERIMENTAL APPARATUS AND PROCEDURE

The annulus is 46 cm deep, and has inner and outer radii of 69.6 and 99.9 cm, respectively, giving a gap Δr of 30.3 cm. The walls are very smooth and their radial distances from the center of the apparatus varies less than 4 mm. Two transparent plastic windows, 20 cm high and 46 cm wide each, are built into the outer wall. A photograph of the apparatus is shown in Fig. II.1. The annulus is mounted on top of a plywood stand to enable a hot-film probe to be inserted from the bottom into the working fluid, which was water.

The water was degassed and filtered prior to each experiment in order to prevent bubble formation and minimize dirt accumulation on hot-film sensors. Initially the annulus was filled with salt water through an inlet on the bottom to the required level, usually 27 cm. Then, a layer of fresh water was gently sprayed from above the annulus to constitute an initial mixed-layer depth, h_0, typically 4 or 5 cm. The initial density difference was 0.04 gm/cm^3 in most of the experiments. In some experiments initial density differences of 0.02 or 0.078 gm/cm^3 were used. The vertical profile of density was measured by a salinity probe at intervals of approximately 100 seconds during each experiment.

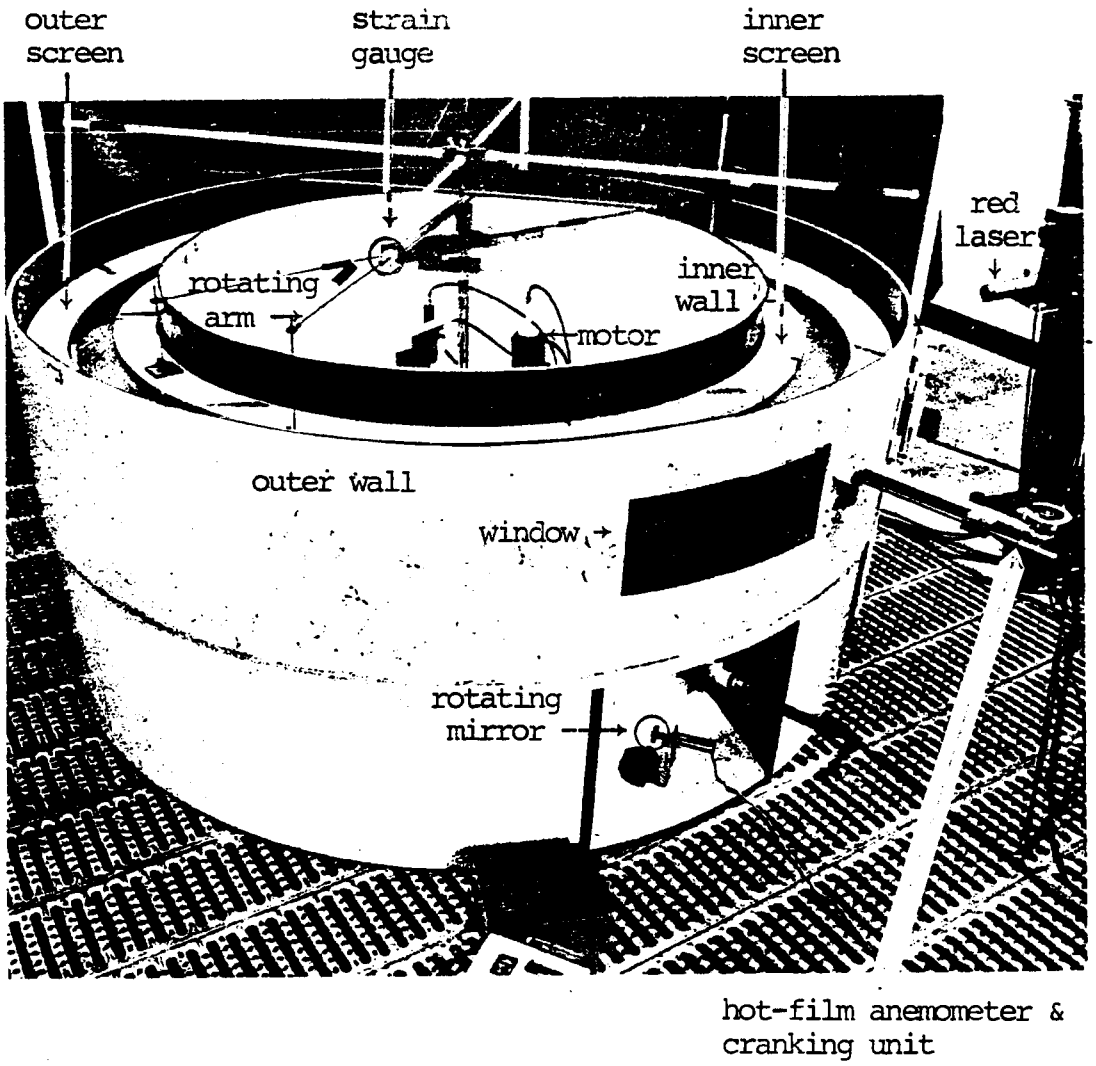

Fig. II.1. Photograph of the experimental apparatus. The screens shown are the inner and the outer ones. In the full-screen mode the middle one (not shown) was added, and then the three screens were connected and rotated by one rotating arm.

The screen is made from a light, flat plastic plate which floats on the water, and is driven by a rotating horizontal arm having its ends connected to two vertical rods mounted on the screen (Fig. II.1). Torque applied to the rotating screen was measured by strain gauges situated

in both sides of the rotating arm. The measured torque was averaged over the entire annulus area and divided by the mean radius to obtain the net surface stress, ρu_*^2. The screen drive system was operated at conditions which resulted in an estimated u_* of 0.8 cm/sec or 1.33 cm/sec. The strain-gauge and other sensor signals were digitized at 20 Hz sampling rate by an analog to digital convertor, and stored on magnetic tape.

Fluorescien (fluorescent dye) was injected into the mixed layer, and its depth (or lower edge of the dye) was measured by monitoring the height of a horizontally-spread red laser beam (0.5 mW) directed through one of the windows in the outer wall. The interface slope associated with centrifugal acceleration was measured by aiming the laser beam alternately at the dye depths near the outer wall and near the inner wall. Visual observations and photography could be made through the other window. The bottom of the annulus near the side window is made of transparent plastic to allow illumination of the interface with a strong (0.5 W) blue laser beam from below. Photographs of the interface across the annulus area were then taken through the side window as the narrow, intense laser beam was scanned radially by rotating a small reflecting mirror located below the annulus.

A hot-film probe was traversed either vertically or horizontally by a cranking system. Probe position was determined using a potentiometer attached to the probe traversing mechanism. The probe position was then read in millimeters on a digital display making it possible to repeat velocity measurements at the same station (location) at a later time. The probe consists of two hot-film sensors positioned as shown below (Fig. II.2).

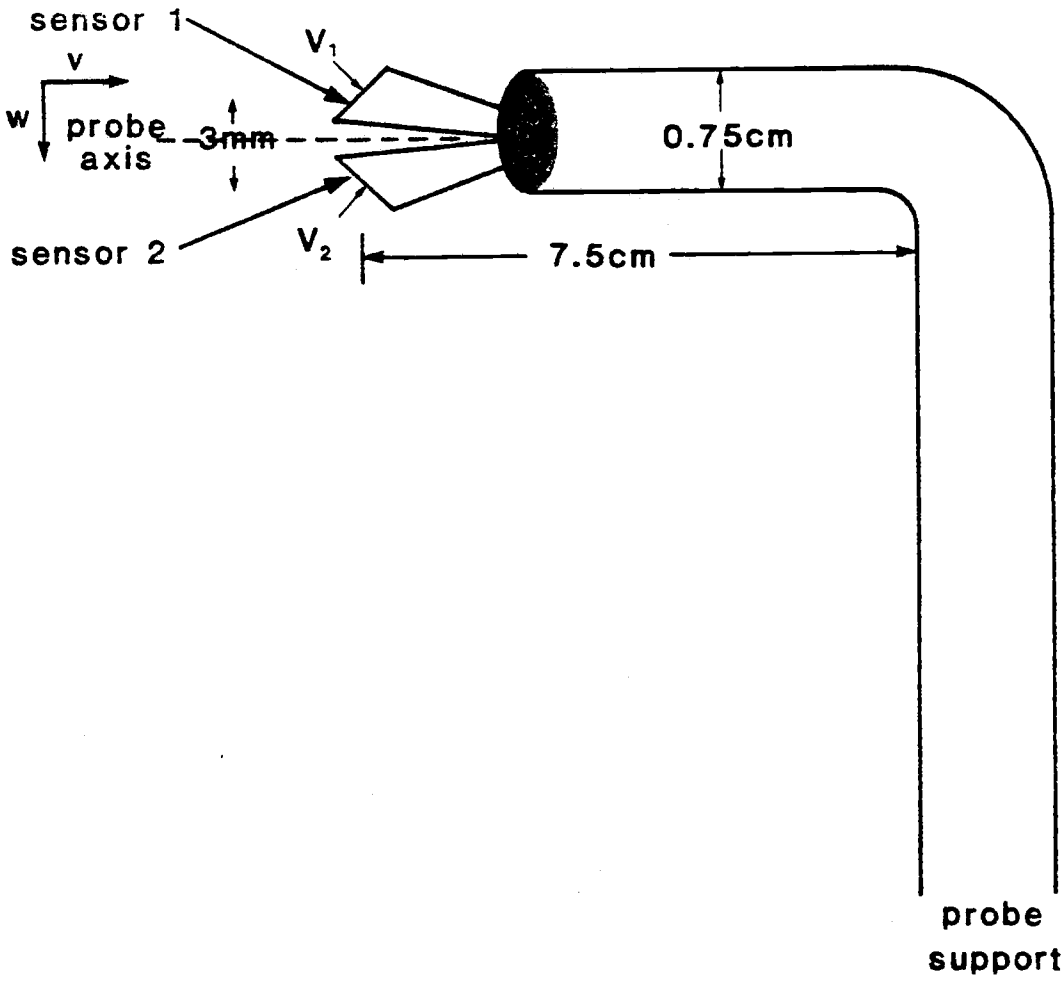

Fig. II.2. Configuration of hot-film anemometer.

When the probe is mounted in the horizontal traversing mechanism the elements measure circumferential speed v and radial speed u (positive outward), and in the vertical traversing mechanism they measure v and vertical speed w (positive downward). Two to six measuring stations were employed, depending upon the goal of each experiment, and two to five replications were made during a single experiment. Hot-film data were taken for 13 seconds at each station before the probe was moved to the next station. Details on the use of the hot-film anemometer follow in the next chapter.

In the full-screen mode, horizontal profiles of the flow were taken at 7 cm below the screen in two experiments (Exps. 1 and 2) and at 1 cm below the screen in two other experiments (Exps. 3 and 4). For protection of the probe its axis was not positioned any closer than 1 cm to the screen. At z=7 cm, the lower part of the secondary circulation and horizontal inhomogeneity of the turbulence intensities near the interface were measured as the interface gradually moved down past the probe height. The mean radial speeds measured at z=1 cm were used to form the upper part of the secondary circulation. In two experiments photographs of particle trajectories were taken alternately at an upper level and at a lower level using a horizontally-spread blue laser beam. About 40

photos with 10 to 20 trajectories each were analyzed to confirm the secondary circulation.

Three experiments (Exps. 5, 6 and 7) in the full-screen mode were conducted to measure vertical profiles at the horizontal center of the annulus area (15 cm from the inner wall). Sampling stations were chosen to be various fractions of h, e.g. 0.2h, 0.5h, 0.9h and 1.1h. For the inner-screen mode three experiments (Exps. 8, 9 and 10) were performed to obtain horizontal profiles at z=4 cm and two experiments (Exps. 11 and 12) to obtain vertical profiles at the horizontal center of the annulus area. Photographs of particle trajectories were also taken, but since the flow is much more turbulent in this mode than in the full-screen mode the particle trajectories could not be traced for the analysis.

III. THE HOT-FILM ANEMOMETRY

III.1 Principle of operation

A hot-film probe is composed of two cylindrical sensors, coated with quartz for use in water. The probe is manufactured by TSI (Thermo-Systems Inc.). The two sensor elements are inclined 45° in each direction from the probe axis thus making a right angle with each other as shown in Fig. II.2. The electrical resistance of the sensor and, accordingly, its temperature are kept constant during measurement. The sensor temperature is usually set 30° - 40°C higher than the fluid temperature. Any variation in temperature and thus in electrical resistance due to the cooling effect of the flow fluctuations is immediately compensated for by means of an electronic feedback system such that the current flow to the sensor is the measure of flow speed. For work in salt water the quartz coating does not affect frequency response until about 30KHz, according to specifications provided by the manufacturer (TSI Manual). Although the total amount of heat transfer depends on many physical variables and fluid properties, for practical purposes, the simplified relationship between the output voltage (compensated by the feedback system) and the mass flux can be stated as

$$E^2/E_0^2 = A + B(\rho V)^n \qquad (1)$$

where E_0 is the reference voltage when there is no mass flux, and A and B are constants depending on the fluid and particular type of sensor, ρ is the density of the fluid, V is the velocity component normal to the sensor, n is an exponent, and E is the output voltage in general. An exponent n=0.51 in air was found by Collis and Williams (1959). In the present work in salt water n=0.30 is found to best fit the relationship (1) for $1.4 < V < 17$ cm/sec. The same value for n in water is reported by Comte-Bellot et al. (1981). The coefficients A and B of each sensor must be determined from daily calibration. If E and E_0 in Eq (1) are known, the effective velocity of each sensor can be computed from

$$V = ((E^2/E_0^2 - A)/B)^{1/n}/\rho \qquad (2)$$

If we assume that the sensors follow a cosine response, the longitudinal component v and lateral component w (or u) of fluid velocity are given by

$$v = (V_1 + V_2)\cos 45^\circ \qquad (3)$$

$$w = (V_1 - V_2)\sin 45^\circ \qquad (4)$$

where the subscript "1" denotes the outer sensor (away from the probe support) and "2" the inner one (see Fig. II.2).

III.2 Anemometer calibration and data processing

The hot-film probe was calibrated in a towing tank, 120 cm long, 25 cm wide, and 40 cm deep in which the probe was towed through the fluid. The probe was held vertically and towed horizontally as shown in Fig. III.1 so that the vertical component of the flow was zero and the horizontal component was the towing speed.

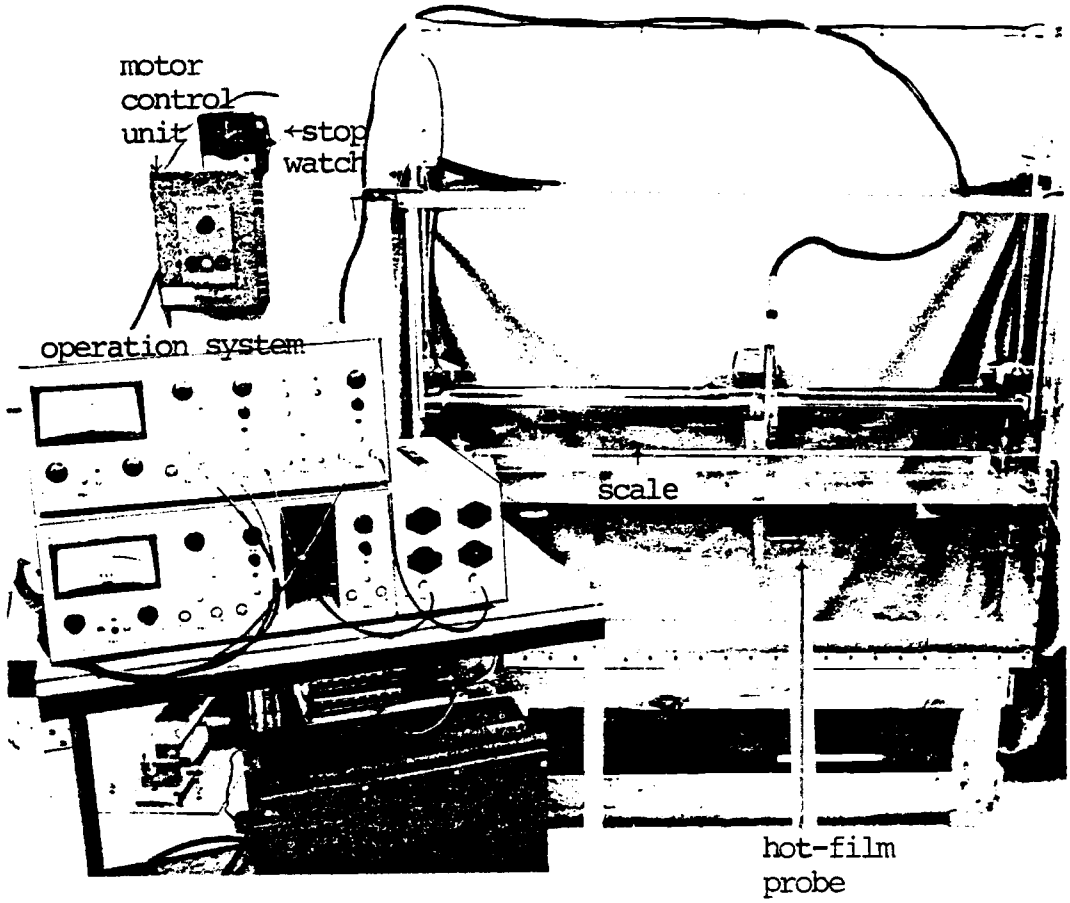

Fig. III.1. Photograph of the towing tank and the hot-film anememeter system.

The towing speed could be varied from 2 cm/sec to 24 cm/sec with a noise level $\sqrt{E'^2}/\bar{E}$ less than 0.5%. Two calibrations were made for each experiment, one before the experiment and the other after the experiment. The coefficients, A and B in Eq (2), for both sensors were determined from the two towing speeds, 2 cm/sec and 24 cm/sec. Averaged coefficients from the two calibrations were used in data processing for each experiment. Typically A was -0.30 ± 0.10 and B was 1.70 ± 0.15 in c.g.s. units.

After the first calibration the probe was inserted into the annulus and remained in water for 4-5 hours until the beginning of the experiment. Any change of the sensors during this period of time could be seen by reading the reference voltages at the beginning of the experiment. These reference voltages were used later in the data processing. Experiments usually ran for about 20-30 minutes. After an experiment the probe was placed back into the towing tank and re-calibrated. Output voltages at this time were usually found to be a few percent less than those of the first calibration. It was thought that this might be caused by dirt accumulated on the sensor surfaces during the experiment.

The errors introduced by a small sensitivity change

were partially eliminated by the data processing procedure, since average coefficients, A and B, were utilized from the before and after calibrations. I. e., we had no information about when or how the changes in sensitivity occurred, whether gradually or abruptly. Strip-chart output showed some changes in the sensor sensitivities, but not to the level of accuracy required to adjust the data. For this sensor which has a low order response as in Eq (2), one must be very careful in correcting the output data. Instead, the results will be interpreted considering the probable errors caused by the sensitivity changes. The maximum sensitivity loss of each sensor could be roughly estimated by comparing reference voltages of the two calibrations (before and after an experiment) with the ones at the beginning of the experiment. From these values the error bounds of the mean velocities and the second moments could be estimated. This will be treated in the next section.

Data processing was performed on the university CDC 6400 computer using a FORTRAN program for analysis. The deviation angle of the probe axis from the tangent line to the arc was computed at each station from a simple geometrical relationship for the horizontal traverses. The corrected angle was used to compute the velocity components in Eqs (3) and (4). This angle was less than

5° in all cases. The hot-film data for each experiment were corrected for this deviation angle. Spectral analyses of the turbulent velocities were performed on several sets of data utilizing a fast Fourier transform (FFT) technique. The analysis completed on the university computer was transmitted over phone lines to our HP-9835 desktop computer for plotting on an HP-9872A graphics plotter for the final analyses.

III.3 Propagation of sensitivity error

Loss of a few percent of the output voltage E leads to 10-20% underestimation of the effective velocity V as the latter is computed from Eq (2). In some experiments the sensitivity losses of the two sensors were found to be significantly different. If d_1 and d_2 are the fractional errors of the true V_1 and V_2, respectively, then values including the errors are

$$\tilde{V}_1 = V_1(1-d_1)$$

$$\tilde{V}_2 = V_2(1-d_2),$$

and since $V_1 \simeq V_2$ in the annulus flow,

$$\tilde{v} = (\tilde{V}_1 + \tilde{V}_2)\cos 45^\circ$$

$$= (V_1 + V_2)\cos 45^\circ - (d_1 V_1 + d_2 V_2)\cos 45^\circ$$

$$\simeq v - v(d_1+d_2)/2$$

$$= v - dv \qquad (5)$$

$$\tilde{w} = (\tilde{V}_1 - \tilde{V}_2)\sin 45^\circ$$

$$= (V_1 - V_2)\sin 45^\circ - (d_1V_1 - d_2V_2)\sin 45^\circ$$

$$\simeq w - v(d_1-d_2)/2$$

$$= w - \Delta v \qquad (6)$$

where values with tildes are the estimated values including sensitivity errors, and $d \equiv (d_1+d_2)/2$ and $\Delta \equiv (d_1-d_2)/2$.

Second moments computed from Eqs (5) and (6), using time averaging (overbars) and deviations (primes) from the averages, will be

$$\overline{\tilde{v}'^2} = \overline{(\tilde{v} - \bar{\tilde{v}})^2}$$

$$= \overline{(v - dv - (\bar{v} - d\bar{v}))^2}$$

$$= (1-d)^2\,\overline{(v - \bar{v})^2}$$

$$\simeq (1-2d)\,\overline{v'^2} \qquad (7)$$

$$\overline{\tilde{w}'^2} = \overline{(\tilde{w} - \bar{\tilde{w}})^2}$$

$$= \overline{((w - \Delta v) - (\bar{w} - \Delta\bar{v}))^2}$$

$$= \overline{(w - \bar{w} - \Delta(v - \bar{v}))^2}$$

$$= \overline{w'^2} + \Delta^2\overline{v'^2} - 2\Delta\overline{v'w'} \tag{8}$$

$$\overline{\tilde{v}'\tilde{w}'} = \overline{(\tilde{v} - \bar{\tilde{v}})(\tilde{w} - \bar{\tilde{w}})}$$

$$= (1-d)\overline{(v - \bar{v})(w - \bar{w} - \Delta(v - \bar{v}))}$$

$$= (1-d)\overline{(v - \bar{v})(w - \bar{w})} - \Delta(1-d)\overline{(v - \bar{v})^2}$$

$$\simeq (1-d)\overline{v'w'} - \Delta\overline{v'^2} \tag{9}$$

For example, if d_1 is 10% and d_2 is 20%, then $\bar{v}$ will be underestimated by 15% from Eq (5), and 5% of $\bar{v}$ will be added to $\tilde{w}$ from Eq (6). Since $\bar{w}$ (or $\bar{u}$, the radial component of fluid velocity) is of order 1 cm/sec or less and $\bar{v}$ is about 15 cm/sec, 5% of $\bar{v}$ can be as big as the true $\bar{w}$ (or $\bar{u}$). From Eq (7) $\overline{v'^2}$ will be underestimated by a factor of 2d. Since $\overline{v'w'}$ (or $\overline{u'v'}$) is considerably smaller than $\overline{v'^2}$ or $\overline{w'^2}$, from Eq (8) $\overline{w'^2}$ will be negligibly affected, while the last term in Eq (9) may change the sign of $\overline{\tilde{v}'\tilde{w}'}$ from that of $\overline{v'w'}$ when the latter is small.

In other words, $\bar{v}$ and $\overline{v'^2}$ are underestimated from their true values by a fraction of d and 2d, respectively, and $\bar{w}$ (or $\bar{u}$) is affected by an additive constant which depends on the difference of the sensitivity losses of the two sensors. The hot-film data presented in the Appendix should be reviewed with consideration of these factors.

III.4 Correction for sensor separation

The two hot-film anemometer sensors are separated by 3 mm from center to center. At the mixed-layer interface the vertical shear in v is quite large. There the difference of effective velocities between the two sensors thus introduces an error to the vertical speed, w, estimated from Eq (4). If v_1 and w_1 were the actual velocity components at the center of sensor 1, and v_2 and w_2 were those at the center of sensor 2, the effective velocities, with or without the shears, can be written from Eq (3) and Eq (4) as

$$V_1 = (v_1 + w_1)/\sqrt{2}$$

$$V_2 = (v_2 - w_2)/\sqrt{2}.$$

Then, v and w computed from these will be

$$v \equiv (V_1 + V_2)/\sqrt{2}$$

$$= (v_1 + v_2)/2 + (w_1 - w_2)/2 \qquad (10)$$

$$w \equiv (V_1 - V_2)/\sqrt{2}$$

$$= (v_1 - v_2)/2 + (w_1 + w_2)/2. \qquad (11)$$

Velocity shear at the entraining interface is typically 10 sec^{-1}, and from Eq (11) this adds an extra speed of 1.5 cm/sec to w. This correction was performed for

$\overline{w}$-profiles near the mixed-layer interface. This effect upon the second moments was not corrected since that introduces second-order errors to them.

III.5 Choice of sampling period

The sampling period should be long enough to include energy containing eddies, and short enough so that the mixed-layer depth does not change significantly (not more than 10%) during the time required to make a horizontal traverse consisting of 4-5 stations. Also, in order to utilize the FFT for spectral analysis, 13s was chosen as an optimum sampling period at each sampling station. With 0.05s as the sampling rate, this gives a time series of at least 256 ($=2^8$) data points at each sampling station.

Near the end of an experiment (Exp. 12) a 260s long data sample was taken at a single station. This time series was used to examine the sampling error introduced by the finite sampling period. These data were divided into twenty 13s or five 52s long series. Power spectra were obtained from the two series of different lengths by utilizing the FFT. The power spectra of 13s samples were averaged over the twenty samples, and the spectra of 52s samples were averaged over the five samples. Comparison of the two resulting spectra (Fig. III.2) shows that the

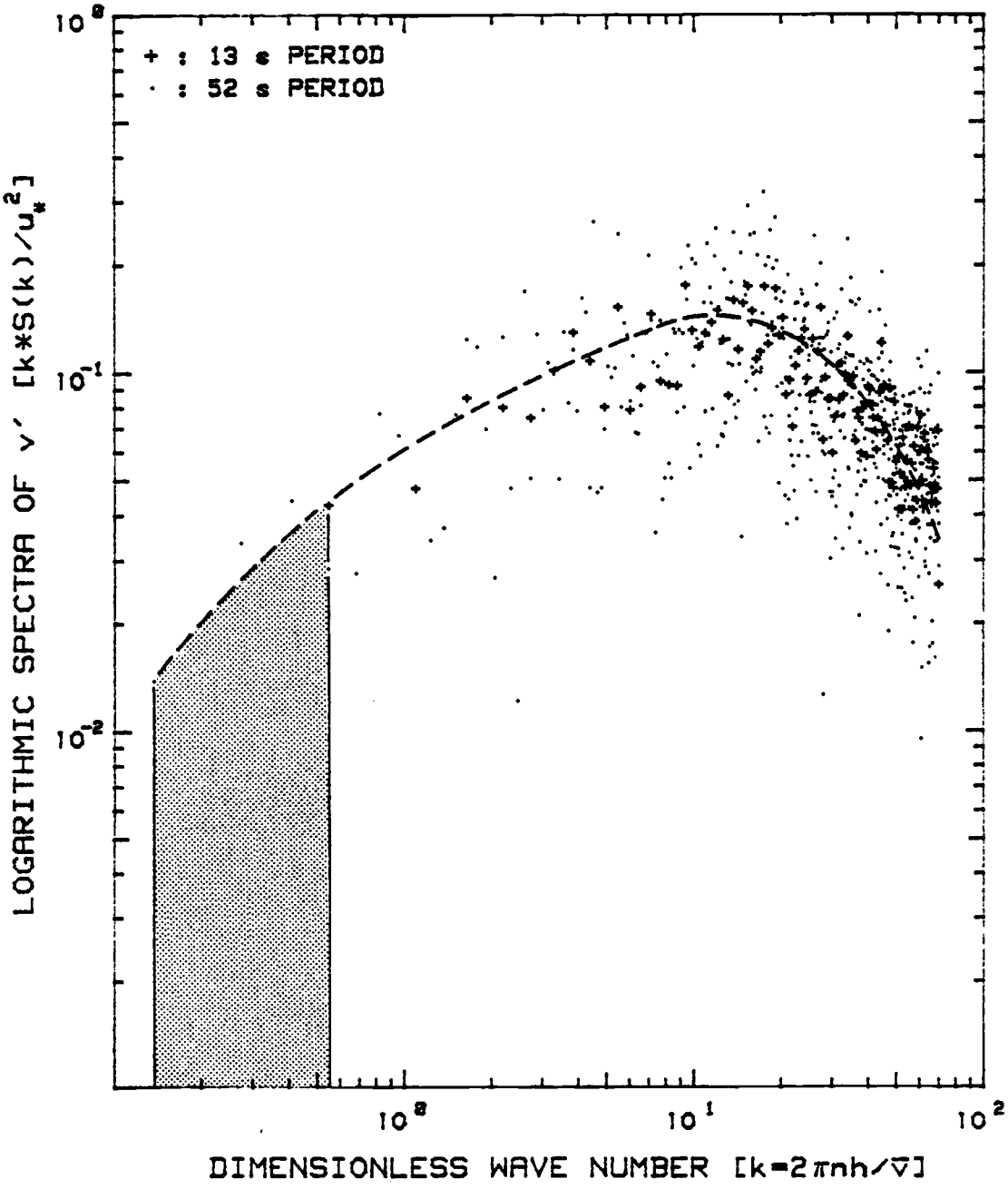

Fig. III.2. The dimesionless logarithmic power spectra of v' for 13s sample period (+) and 52s sample period (·).

13s data contains 90% of the turbulent kinetic energy of the 52s data.

The error introduced by the finite sampling period can be estimated in another way. Let v' be the instantaneous fluctuation velocity with respect to the ensemble average <v>, and v" be the fluctuation with respect to a 13s average $\overline{v}$. Then,

$$v = v' + \langle v \rangle = v'' + \overline{v}$$

and

$$\begin{aligned}
\overline{\langle v' \rangle^2} &= \overline{\langle (v - \langle v \rangle)^2 \rangle} \\
&= \overline{\langle (v'' + \overline{v} - \langle v \rangle)^2 \rangle} \\
&= \overline{\langle v'' \rangle^2} + \langle (\overline{v} - \langle v \rangle)^2 \rangle + 2\, \overline{\langle v''(\overline{v} - \langle v \rangle) \rangle} \\
&= \overline{\langle v'' \rangle^2} + \langle (\overline{v} - \langle v \rangle)^2 \rangle - 2\, \overline{\langle v'' \langle v \rangle \rangle}
\end{aligned} \tag{12}$$

where an overbar denotes a 13s average. The last term in Eq (12) will be zero if there is no trend, or it will be small unless the trend is very steep during a 13s sample period. In practice the ensemble average may be evaluated by the arithmetic mean of N realizations, where N will be twenty for 13s data, and five for 52s data in the present test. Then, Eq (12) becomes

$$\overline{\overline{v'}^2} = \overline{\overline{v''}^2} + \overline{\overline{v}}^2 - \overline{\overline{v}}^2 \tag{13}$$

where an upper bar denotes the arithmetic-mean approximation to the ensemble average. Similarly,

$$\overline{w'^2} = \overline{w''^2} + \overline{\bar{w}^2} - \overline{\bar{w}}^2 \tag{14}$$

$$\overline{v'w'} = \overline{v''w''} + \overline{\bar{v}\bar{w}} - \overline{\bar{v}}\,\overline{\bar{w}}. \tag{15}$$

Application of Eq (13) to the time series mentioned above shows in Table III.1 that $\overline{\bar{v}'^2}$ is enhanced by 25% from the value of $\overline{\bar{v}''^2}$ representing the 13s data and by 6% from the value of $\overline{\bar{v}''^2}$ representing the 52s data. Therefore, a 13 s sample period introduces a finite sampling error less than 25% which is acceptable considering its advantage of providing a full horizontal traverse before the mixed-layer depth changes significantly. No correction was made for this effect. The time series used for this analysis was taken from an inner-screen mode in which the flow is much more turbulent than in the full-screen mode.

Table III.1. Comparison of the sampling errors of the two finite sample periods. A 260s time series is divided into twenty 13s series and five 52s series. Their arithmetic-mean approximations to the ensemble average show that the finite-period sampling error of 13s sample period is 20% and that of 52s sample period is 6%.

13s time series

n	$\bar{v}$	$\overline{v''^2}$
1	11.49	.6517
2	11.25	.3730
3	11.27	.6686
4	11.59	.5972
5	11.81	.8585
6	11.23	1.0514
7	11.45	.5417
8	11.11	.6915
9	11.24	.6611
10	11.22	.5874
11	11.22	.6764
12	10.93	.4539
13	11.13	.5646
14	10.93	.4181
15	11.01	.3685
16	10.96	.5464
17	10.82	.3965
18	10.86	.4700
19	11.29	.6155
20	10.86	.5556

$\bar{\bar{v}} = 11.18$ $\bar{\overline{v''^2}} = .5874$

$\overline{\bar{v}^2} = 125.14$

$\overline{\overline{v'^2}} = \bar{\overline{v''^2}} + \overline{\bar{v}^2} - \bar{\bar{v}}^2$

$= .7350$

52s time series

n	$\bar{v}$	$\overline{v''^2}$
1	11.40	.5939
2	11.40	.8555
3	11.15	.6116
4	11.01	.4802
5	10.96	.5458

$\bar{\bar{v}} = 11.18$ $\bar{\overline{v''^2}} = .6174$

$\overline{\bar{v}^2} = 125.12$

$\overline{\overline{v'^2}} = \bar{\overline{v''^2}} + \overline{\bar{v}^2} - \bar{\bar{v}}^2$

$= .6525$

IV. INTERPRETATION OF EXPERIMENTAL RESULTS

IV.1 Inertial stability

The experimental results may be interpreted in terms of inertial stability. This section will review the horizontal stability criterion for the flow in the annulus. The equations for an incompressible fluid in cylindrical coordinates, z increasing downward, are

$$\frac{du}{dt} = \frac{v^2}{r} - \frac{1}{\rho_o}\frac{\partial p}{\partial r} + \nu(\nabla^2 u - \frac{u}{r^2} - \frac{2}{r^2}\frac{\partial v}{\partial \theta}) \tag{16}$$

$$\frac{dv}{dt} = -\frac{uv}{r} - \frac{1}{\rho_o}\frac{\partial p}{\partial \theta} + \nu(\nabla^2 v - \frac{v}{r} + \frac{2}{r^2}\frac{\partial u}{\partial \theta}) \tag{17}$$

$$\frac{dw}{dt} = \frac{\rho}{\rho_o} g - \frac{1}{\rho_o}\frac{\partial p}{\partial z} + \nu\nabla^2 w \tag{18}$$

$$\frac{\partial u}{\partial r} + \frac{u}{r} + \frac{1}{r}\frac{\partial v}{\partial \theta} + \frac{\partial w}{\partial z} = 0 \tag{19}$$

where the Boussinesq approximation is assumed, i.e. $\rho(x,t) = \rho_o + \rho'(x,t)$, and

$$\frac{d}{dt} \equiv \frac{\partial}{\partial t} + u\frac{\partial}{\partial r} + \frac{v}{r}\frac{\partial}{\partial \theta} + w\frac{\partial}{\partial z} \quad ,$$

$$\nabla^2 \equiv \frac{\partial^2}{\partial r^2} + \frac{1}{r}\frac{\partial}{\partial r} + \frac{1}{r^2}\frac{\partial^2}{\partial \theta^2} + \frac{\partial^2}{\partial z^2} \quad .$$

For an axisymmetric inviscid flow Eq (17) becomes

$$\frac{dv}{dt} + \frac{uv}{r} = \frac{1}{r}\frac{drv}{dt} = \frac{1}{r}\frac{dL}{dt} = 0 \qquad (20)$$

That is, the angular momentum L(=rv) is conserved along the motion of the fluid. If a fluid element situated at $r = r_1$, with $L_1 = r_1 v_1$, is moved to $r = r_2 > r_1$, the centrifugal acceleration it experiences at its new position is L_1^2/r_2^3, whereas the pressure gradient force per unit mass at $r = r_2$ is still L_2^2/r_2^3, where $L_2 = r_2 v_2$ is the angular momentum of the fluid element originally situated at $r = r_2$. If $L_1 < L_2$, the pressure gradient force is greater than the centrifugal force of the displaced element, and will therefore push it back toward $r = r_1$. Hence the fluid is stable if L (r) increases with r and unstable if L (r) decreases with r. This is Rayleigh's (1916) stability criteria of an inviscid fluid for an axisymmetric disturbances. According to Taylor's (1923) work on the stability of a viscous fluid between two concentric cylinders, the inviscid theory is applicable to viscous fluid except that when the outer cylinder is rotating in the opposite direction to the inner one, the speed of the inner cylinder at which the instability sets in is greater than what it would be if the outer cylinder were at rest. In the annulus experiment the screen is rotating in one direction, and the outer wall is at rest (as is inner wall).

IV.2 Flow structure in full-screen mode

The hot-film data of the twelve experiments conducted for this study are listed in Table A in the Appendix. They give: 1) the time at which the sampling period began, 2) mean mixed-layer depth over the 13s period, 3) radial or vertical position of the probe, 4) 13s averages of the velocity components and the second moments. Selected data points from Table A are plotted in Figs. IV.1 - IV.18 below. For each experiment a few full traverses were chosen from the replications of a number of sampling stations. Data near the beginning of each experiment, but after the mean flow speed $\overline{v}$ reached its maximum, were preferred over those near the end since the earlier data had less chance of having significant sensitivity changes due to surface contamination of the probe. The dashed lines in the figures are the eyeball averages. Dashed-line extrapolations indicate known trends which must occur.

The horizontal profiles of the flow at the lower level (z=7 cm) of the mixed-layer were measured in Exps. 1 and 2. The hot-film data for these experiments are listed in Tables A.1 and A.2. Seleted data from these tables are plotted in Figs. IV.1a-IV.6a. The circumferential component, $\overline{v}$, of the mean flow in Fig. IV.1a and the mean

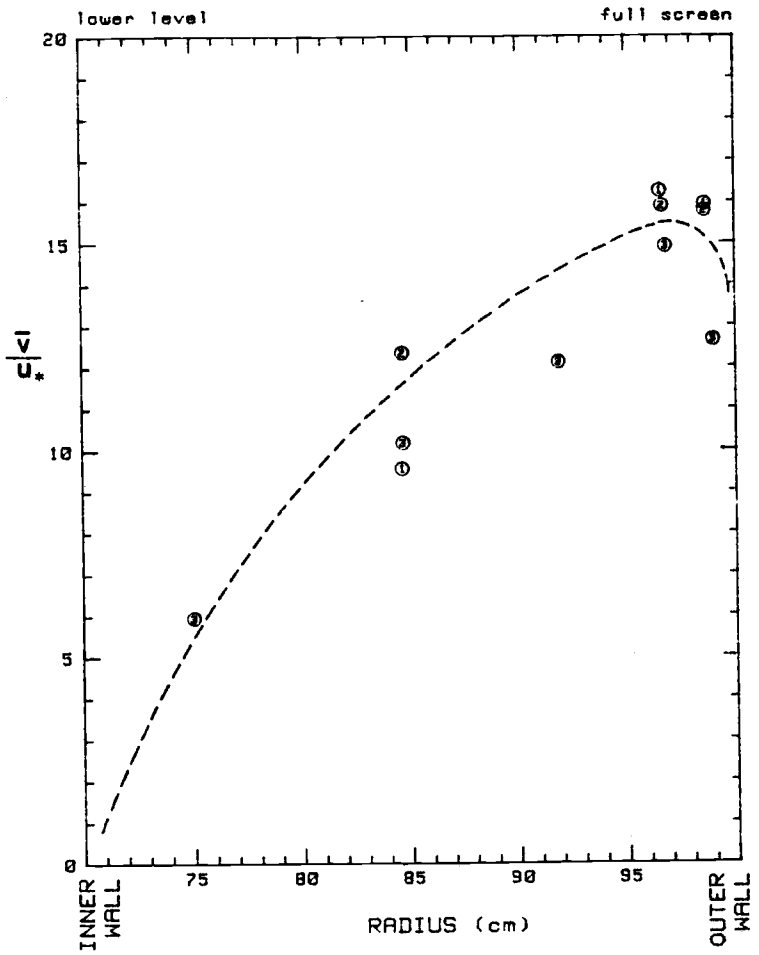

Fig. IV.1a. Horizontal profile of $\bar{v}/u_*$ at z=0.9h in the full-screen mode.

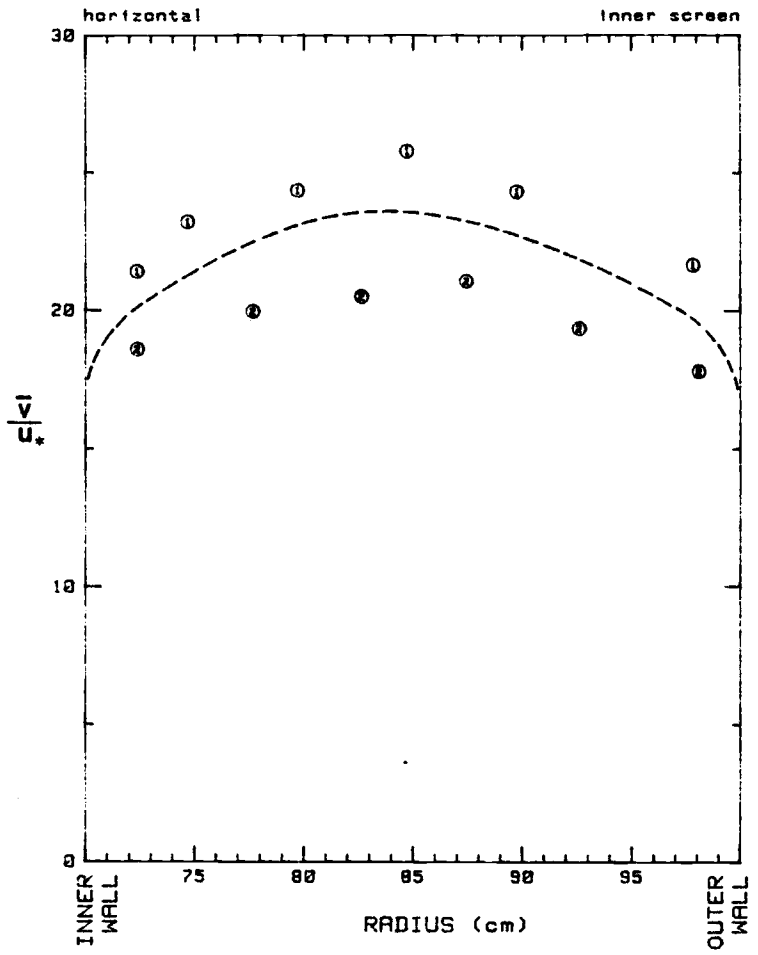

Fig. IV.1b. Horizontal profile of $\bar{v}/u_*$ at z=0.5h in the inner-screen mode.

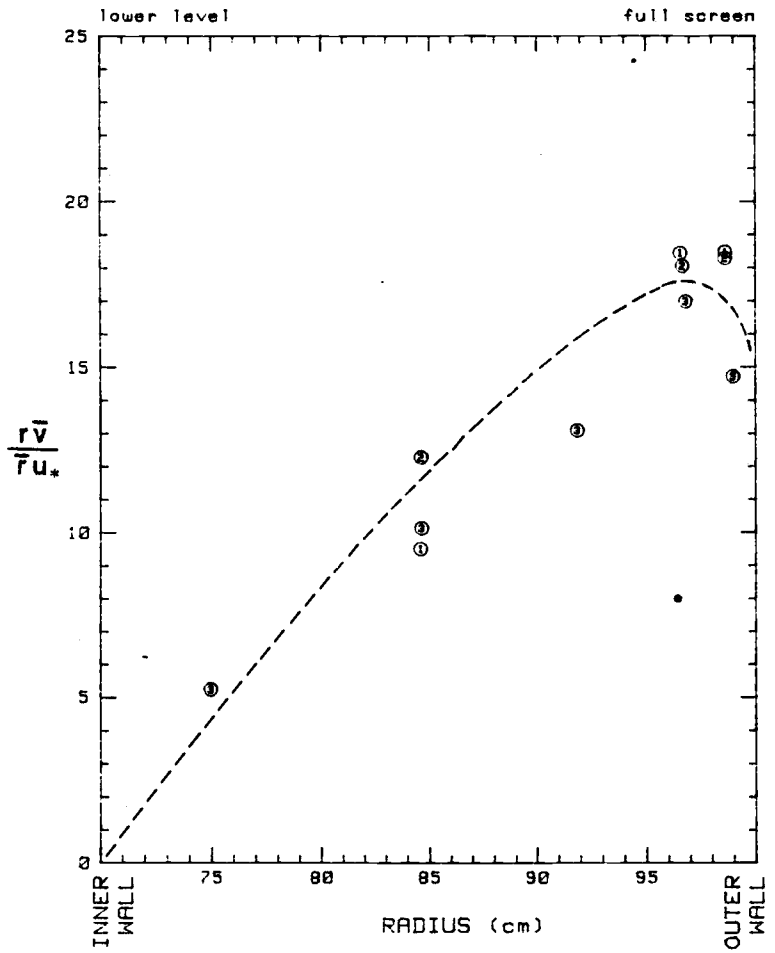

Fig. IV.2a. Horizontal profile of $\bar{r}\bar{v}/\bar{r}u_*$ at z=0.9h in the full-screen mode.

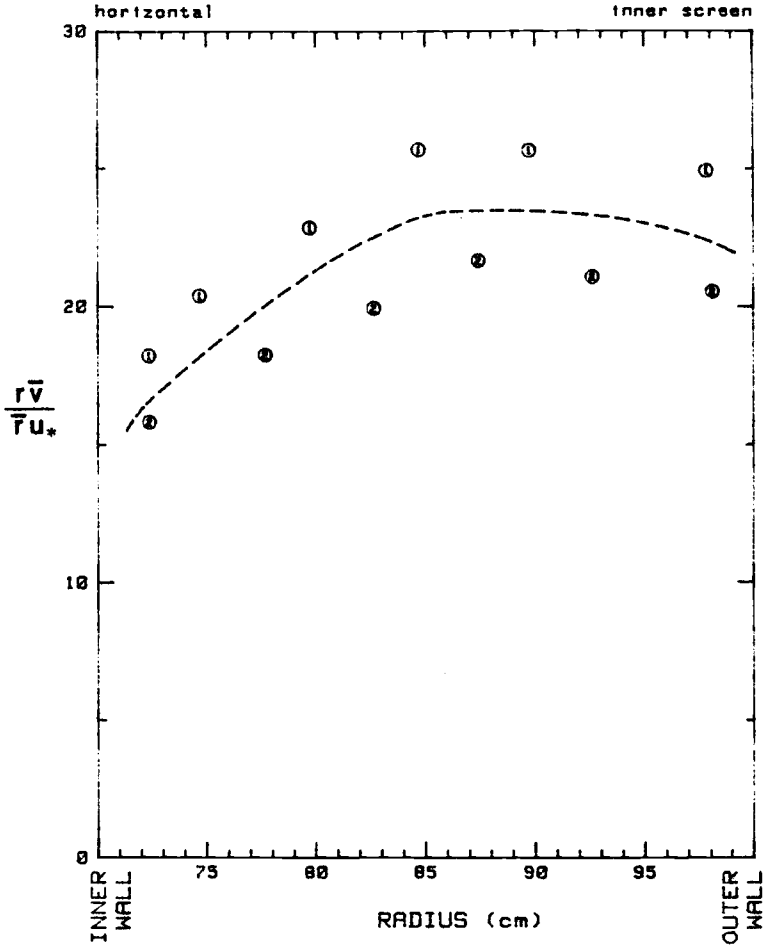

Fig. IV.2b. Horizontal profile of $\bar{r}\bar{v}/\bar{r}u_*$ at z=0.5h in the inner-screen mode.

angular momentum, $\overline{L}(=\overline{rv})$, in Fig. IV.2a increase with radius except in the narrow region near the outer wall (hereinafter referred to as 'outer-wall layer'). This means that the flow is inertially stable at this level except in the outer-wall layer, and therefore any axisymmetric disturbances introduced into the central region will tend to be damped out. While the inertial-stability argument applies strictly to axisymmetric disturbances, it is presumed that non-axisymmetric disturbances will be damped too, if they are elongated in the downstream (θ) direction. Since such disturbances are believed to exist prominently in shear-stress driven flows, where they are called roll vortices or Langmuir cells (Faller, 1971), they are believed present in these experiments, too, to the extent that they are not damped out.

In the outer-wall layer the non-slip condition of a real fluid requires the mean velocity (and therefore angular momentum) to decrease abruptly in that region so that the flow there may be unstable inertially. The measured turbulent intensities in the outer-wall layer are greater than those in the inertially stable region by an order of magnitude, supporting this possibility (Figs. IV.3a and IV.4a). Therefore, the entrainment does not occur uniformly across the horizontal area. This

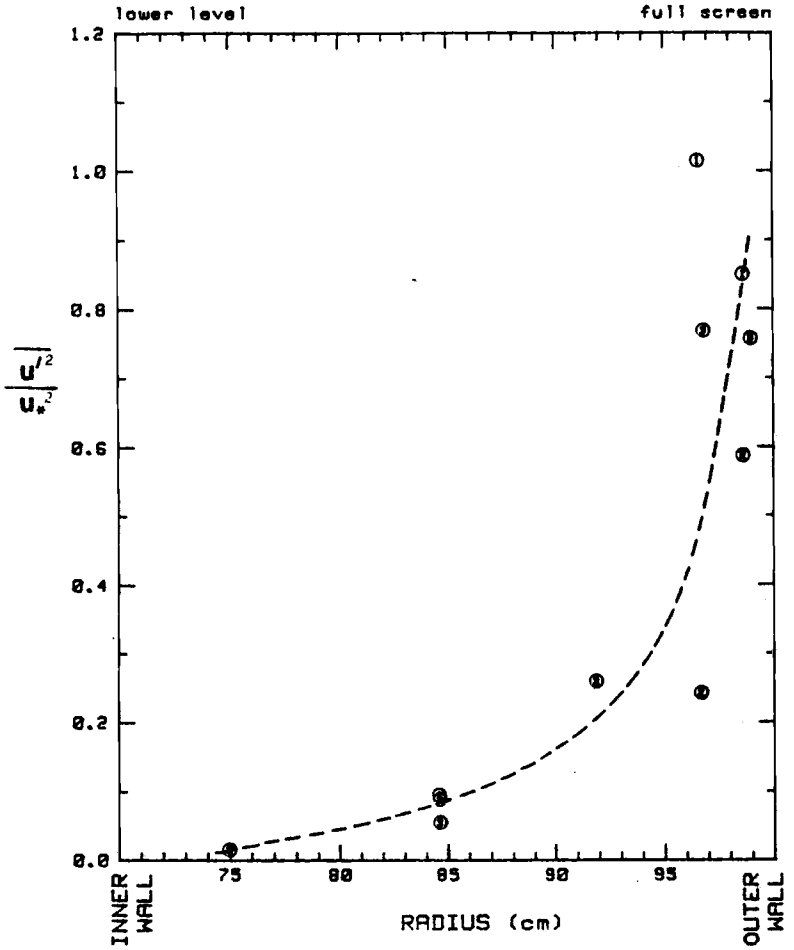

Fig. IV.3a. Horizontal profile of $\overline{u'^2}/u_*^2$ at z=0.9h in the full-screen mode.

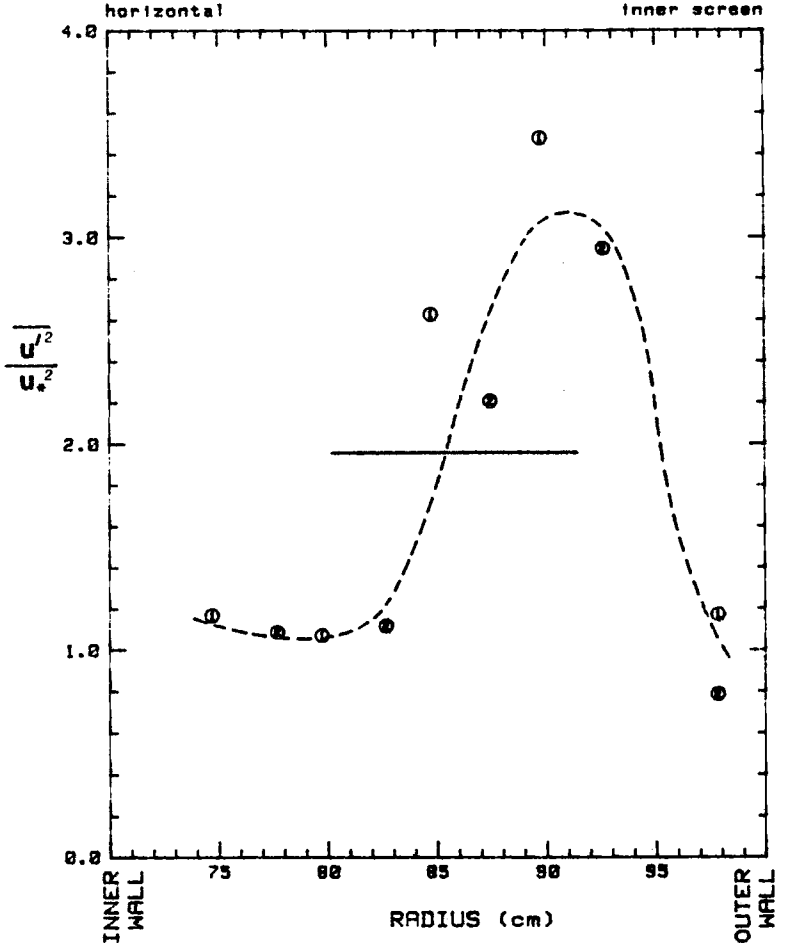

Fig. IV.3b. Horizontal profile of $\overline{u'^2}/u_*^2$ at z=0.5h in the inner-screen mode. The solid line is the average value across the annulus area.

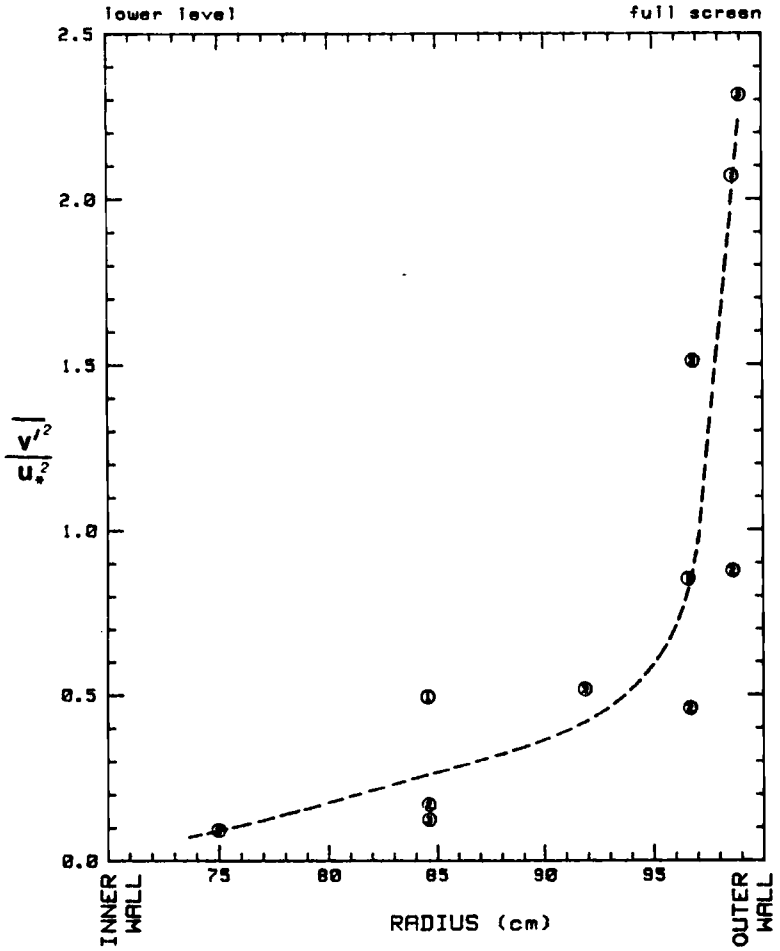

Fig. IV.4a. Horizontal profile of $\overline{v'^2}/u_*^2$ at z=0.9h in the full-screen mode.

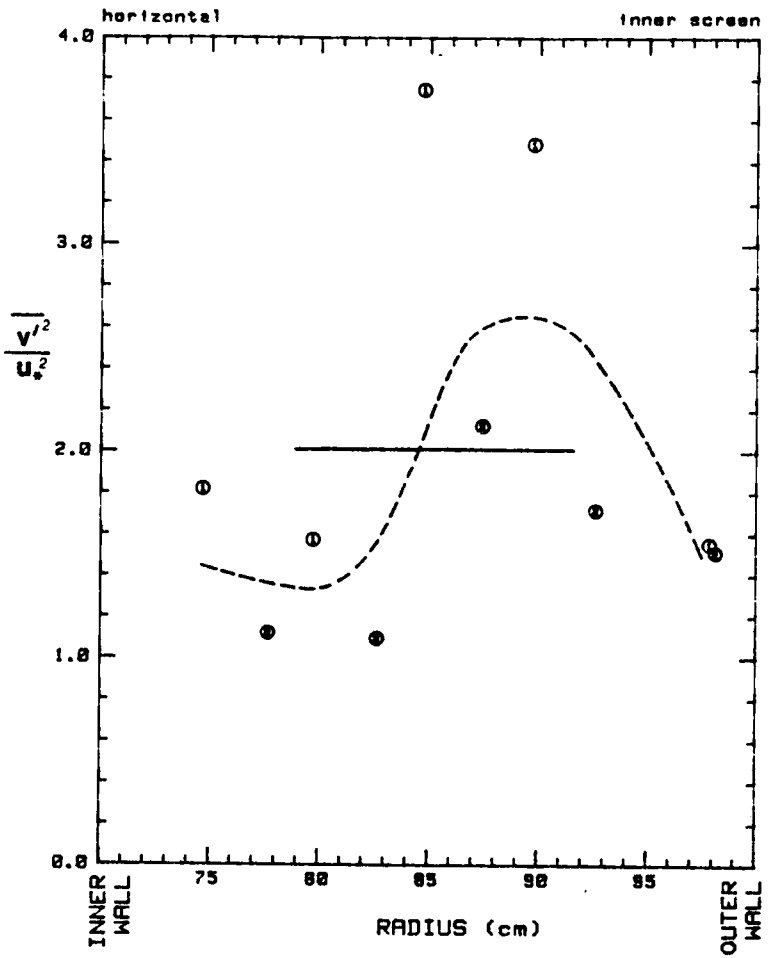

Fig. IV.4b. Horizontal profile of $\overline{v'^2}/u_*^2$ at z=0.5h in the inner-screen mode. The solid line is the average value across the annulus area.

implies that the flow properties in this screen-drive mode do not reflect the one-dimensional entrainment process which is assumed to occur in geophysical flows of large horizontal extent.

The Reynolds stress $\overline{u'v'}$ given in Fig. IV.5a is negative so that the turbulent motion transports the momentum inward. The radial component, $\bar{u}$, of the mean velocity shown in Fig. IV.6a is also negative, which means that the turbulence of considerably greater intensity in the outer-wall layer is advected inward by the secondary ciculation. By comparing their magnitudes we can see that the inward transport by the Reynolds stress is negligible compared to the transport by the secondary circulation. The large value of $\bar{u}$ near the outer wall is associated with mass continuity which will be described later in this section. Care was taken in selecting the mean radial velocities for the plots. From the set of experiments having the same conditions, the data having smallest differences of the sensitivity changes of the two sensors were selected (see section III.3).

A very low speed, apparently laminar, flow is usually observed in a wedge-shaped region near the inner wall. Existence of a wedge region and outer-wall layer was reported by Scranton and Lindberg (1982). The mean

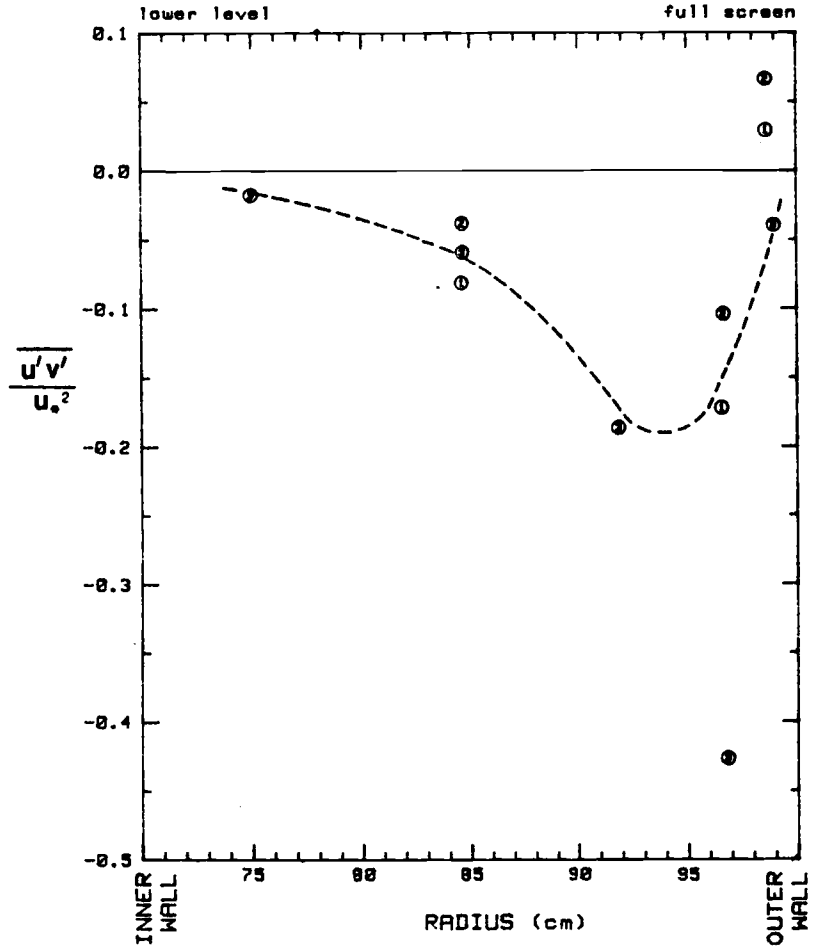

Fig. IV.5a. Horizontal profile of $\overline{u'v'}/u_*^2$ at z=0.9h in the full-screen mode.

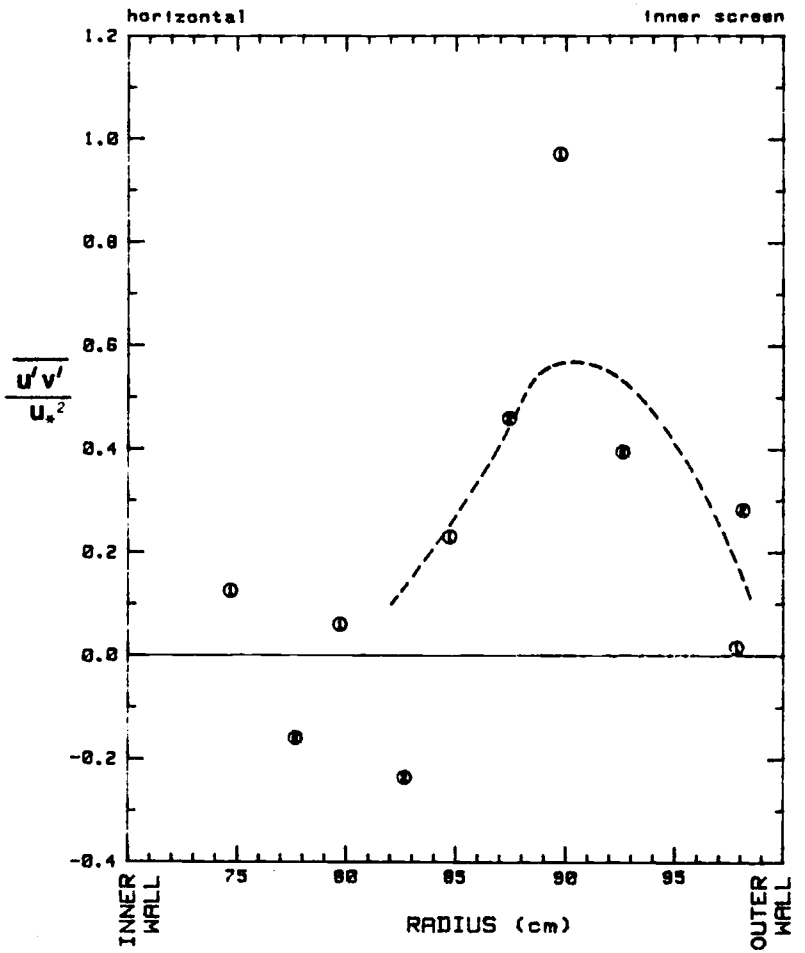

Fig. IV.5b. Horizontal profile of $\overline{u'v'}/u_*^2$ at z=0.5h in the inner-screen mode.

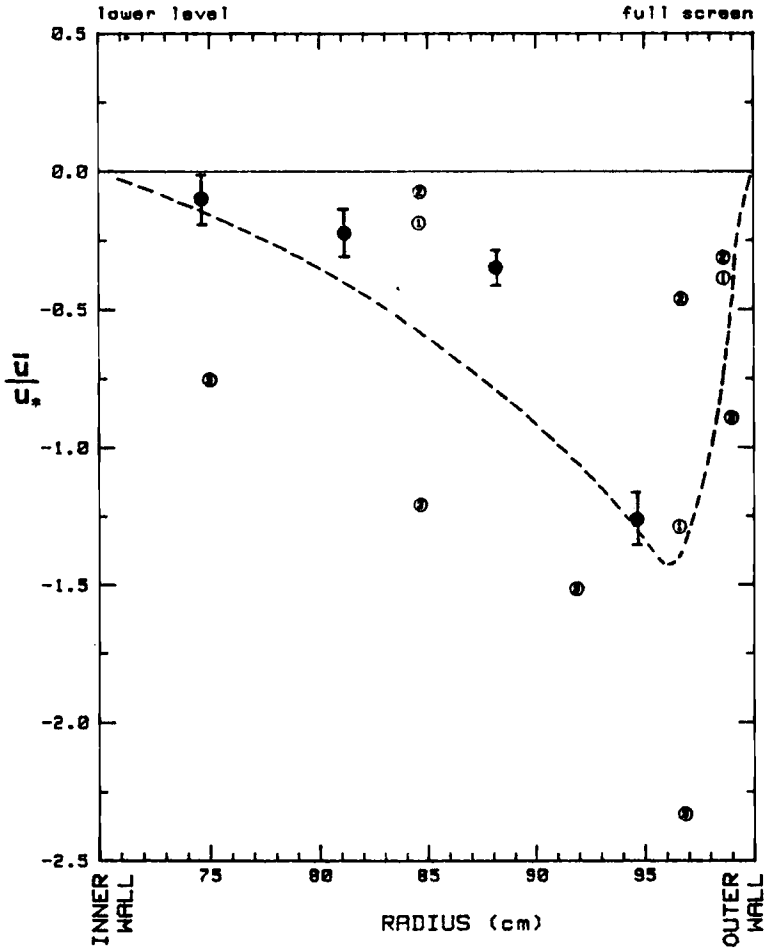

Fig. IV.6a. Horizontal profile of $\bar{u}/u_*$ at z=0.9h in the full-screen. The dark circles are the averaged particle speeds with their standard deviations (error bars).

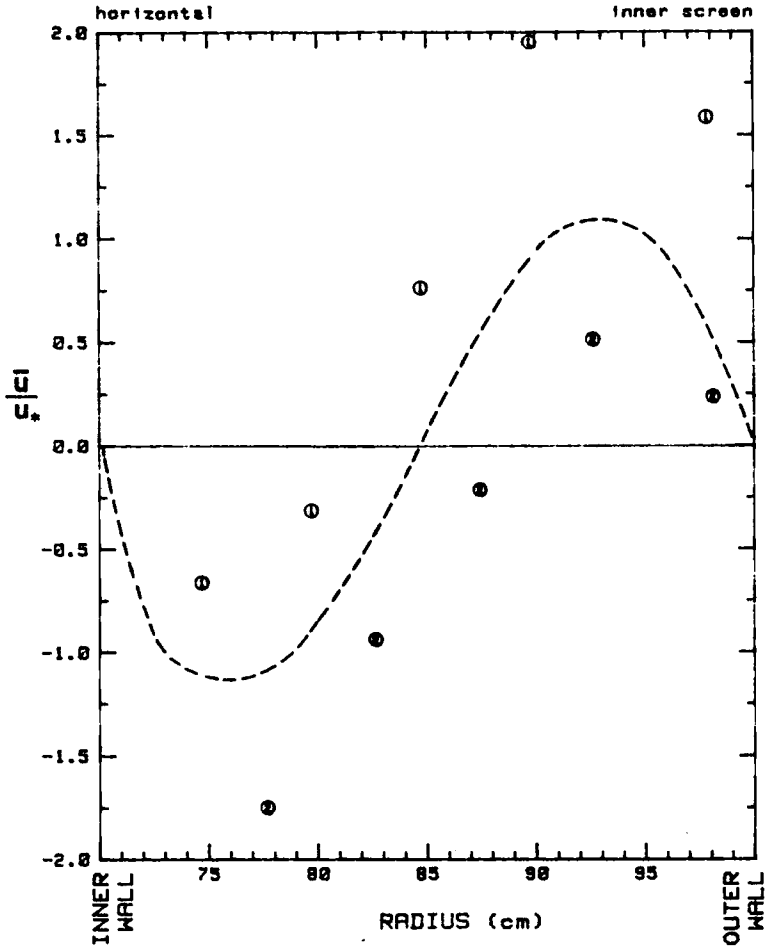

Fig. IV.6b. Horizontal profile of $\bar{u}/u_*$ at z=0.5h in the inner-screen mode.

velocity profile near the bottom of the wedge in Fig. IV.1a supports the contention that the flow is laminar there. In that region the mean velocity distribution is nearly parabolic similar to that for Poiseuille flow through a channel with flat walls (Schlichting, 1979 page 280). The wedge region was also inferred from the particle trajectories of which photographs are shown in Fig. IV.7. Particles of the same density as the mixed-layer fluid were injected to the mixed layer near the inner wall. They moved out of the wedge region very quickly, and never returned there. This implies that the fluid density in the wedge region is larger than that in the rest of the mixed layer. The upper photo in Fig. IV.7 shows the particles throughout the entire annulus area at z=0.11h, while the lower one at z=0.88h shows that the particles have been transported out from the inner 1/3 of the annulus area. Higher density fluid in the wedge region suggests that the secondary circulation drags some of the denser lower fluid toward the inner wall, and the turbulence in the mixed layer is not sufficient to fully mix this denser fluid with the mixed-layer fluid.

The flow properties at the upper level (z=1 cm) of the mixed layer were measured in Exps. 3 and 4. Tables A.3 and A.4 contain the hot-film data for these

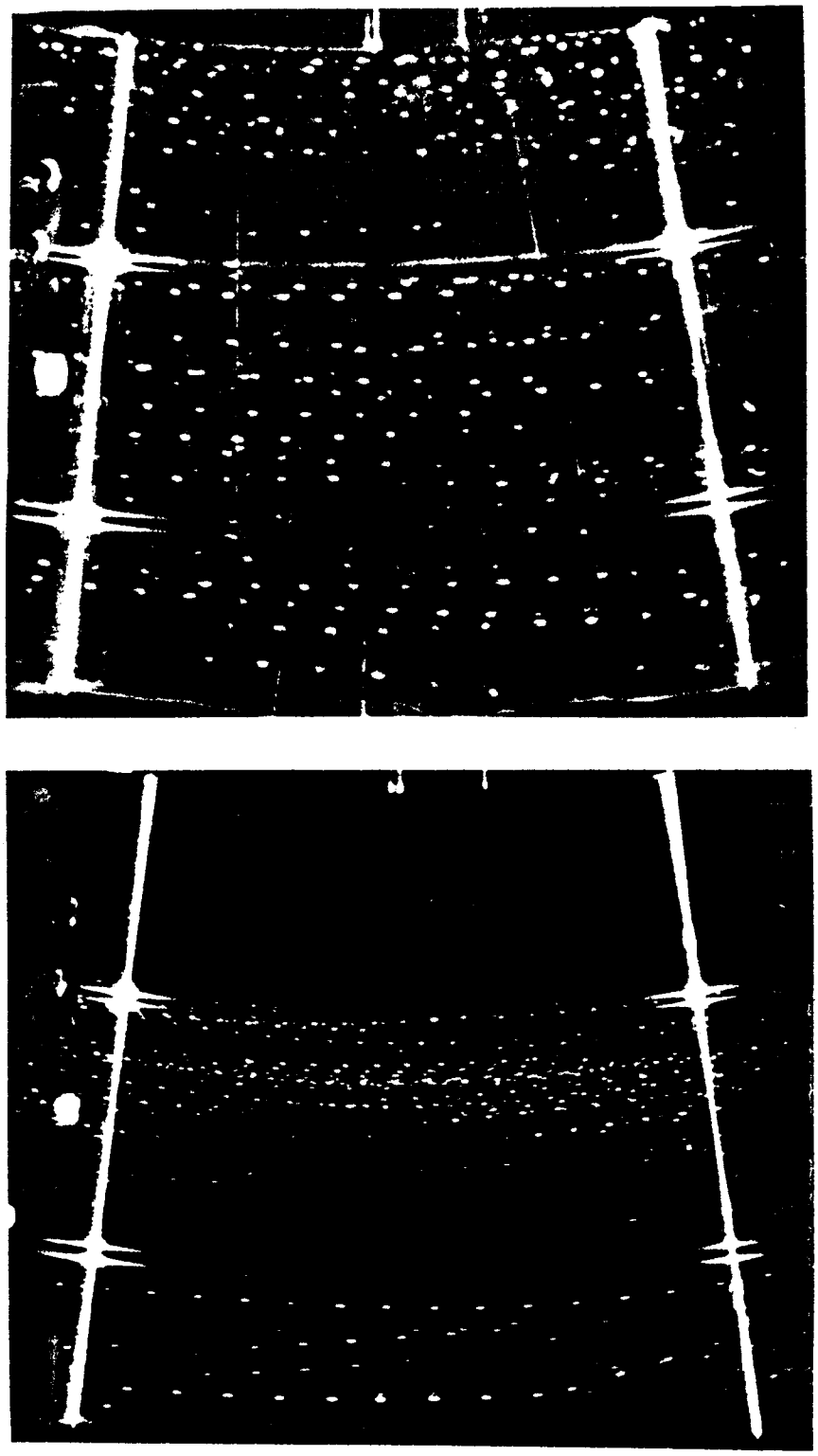

Fig. IV.7. Photographs of the particle trajectories in the full-screen mode: the upper one is at z=0.11h, and the lower one is at z=0.88h (h=6.9 cm). The particles are moving to the right in the photos. The time interval from one point to the next is 1/8 sec.

experiments, and Figs. IV.8 - IV.13 present a plot of representative data from these tables. The mean velocity component $\overline{v}$ is rather uniform everywhere except in the area close to each wall as shown in Fig. IV.8. The mean angular momentum given in Fig. IV.9 shows that the flow inertial stability is much weaker than that at the lower level (Fig. IV.2a) throughout most of the annulus area. The turbulent intensities shown in Figs. IV.10 and IV.11 are also rather homogeneous and much larger than those at the lower level. These suggest that the flow at this depth is directly influenced by the surface stress applied by the rotating screen. The values of the second moments near the inner wall are not plotted, because they are suspected to have been influenced significantly by the mechanical vibration of the probe as a greater length of the probe support is subject to the high speed flow here.

$\overline{u'v'}$ is mainly positive, and $\overline{u}$ is also mostly positive, increasing with radius (Figs. IV.12 and IV.13). In contrast to the flow at the lower level, $\overline{u}$ transports the momentum outward at this level, suggesting a cell type circulation in the mixed layer. The negative value of $\overline{u}$ near the inner wall may represent the returning flow that has not changed its direction yet at this position while it has changed the direction toward the outer wall in the area where r is greater than 80 cm.

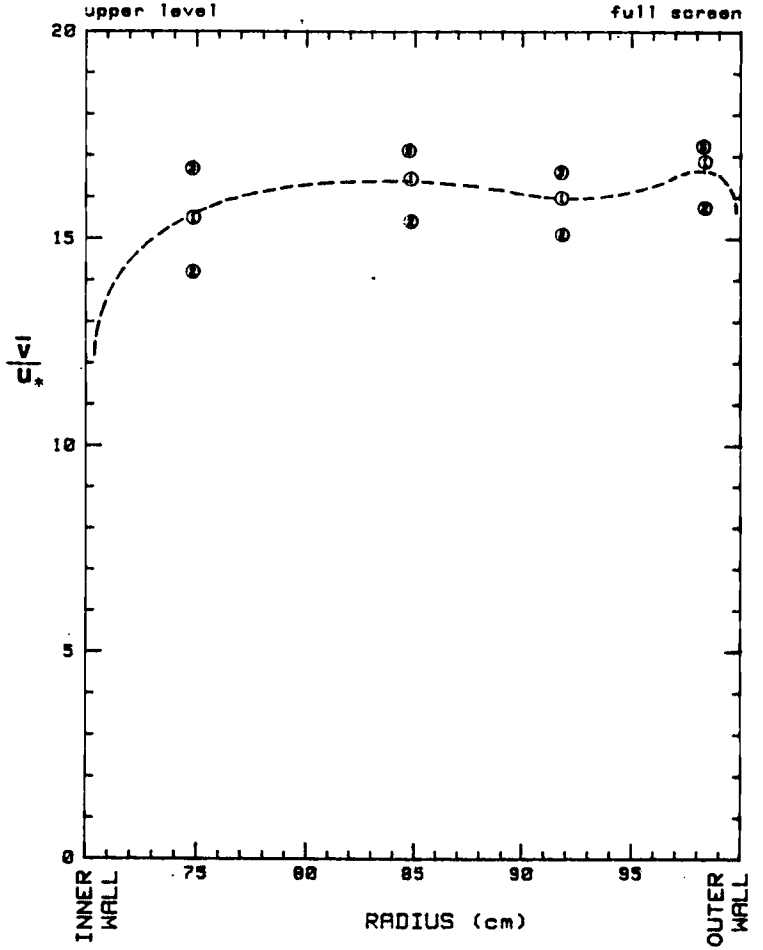

Fig. IV.8. Horizontal profile of $\bar{v}/u_*$ at z=0.17h in the full-screen mode.

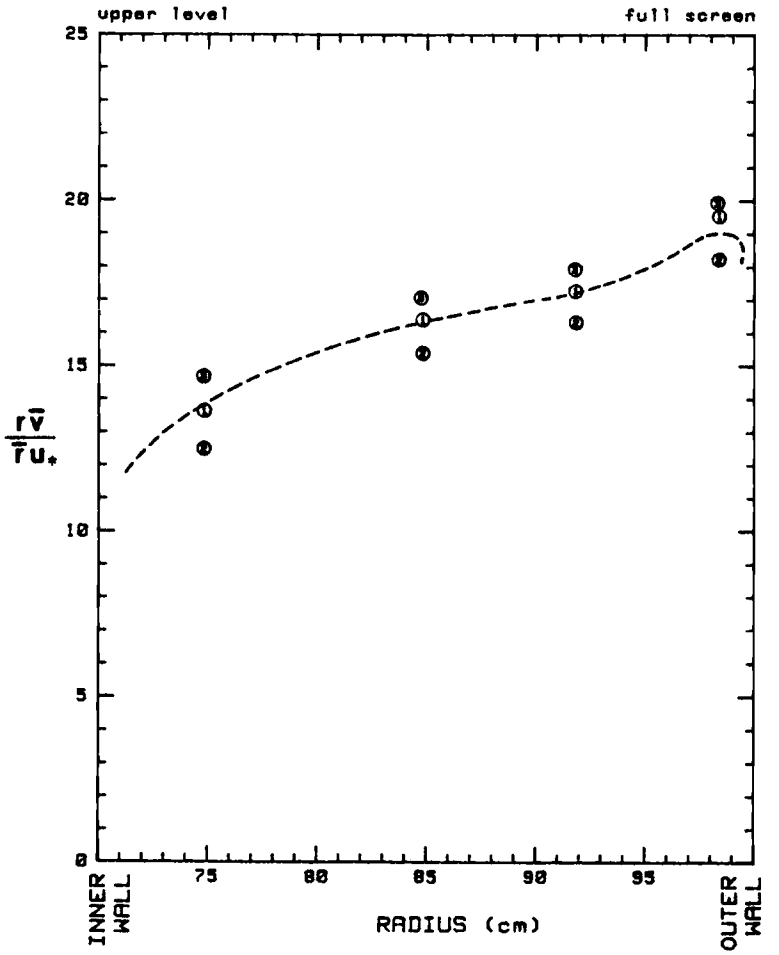

Fig. IV.9. Horizontal profile of $\bar{r}\bar{v}/\bar{r}u_*$ at z=0.17h in the full-screen mode.

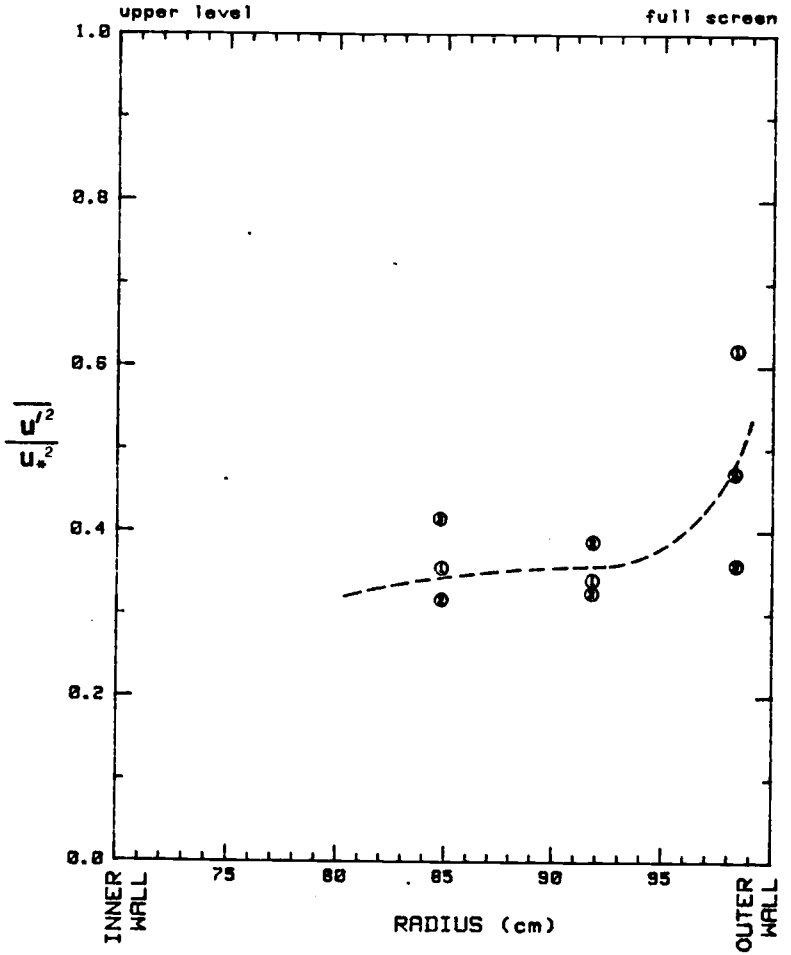

Fig. IV.10. Horizontal profile of $\overline{u'^2}/u_*^2$ at z=0.17h in the full-screen mode.

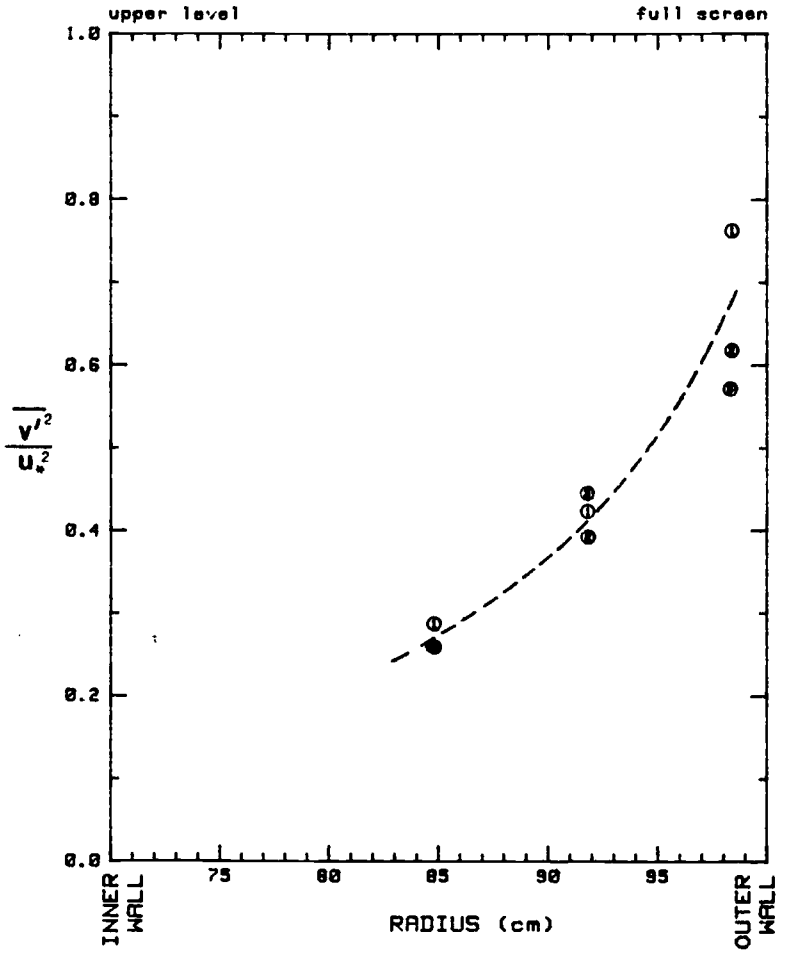

Fig. IV.11. Horizontal profile of $\overline{v'^2}/u_*^2$ at z=0.17h in the full-screen mode.

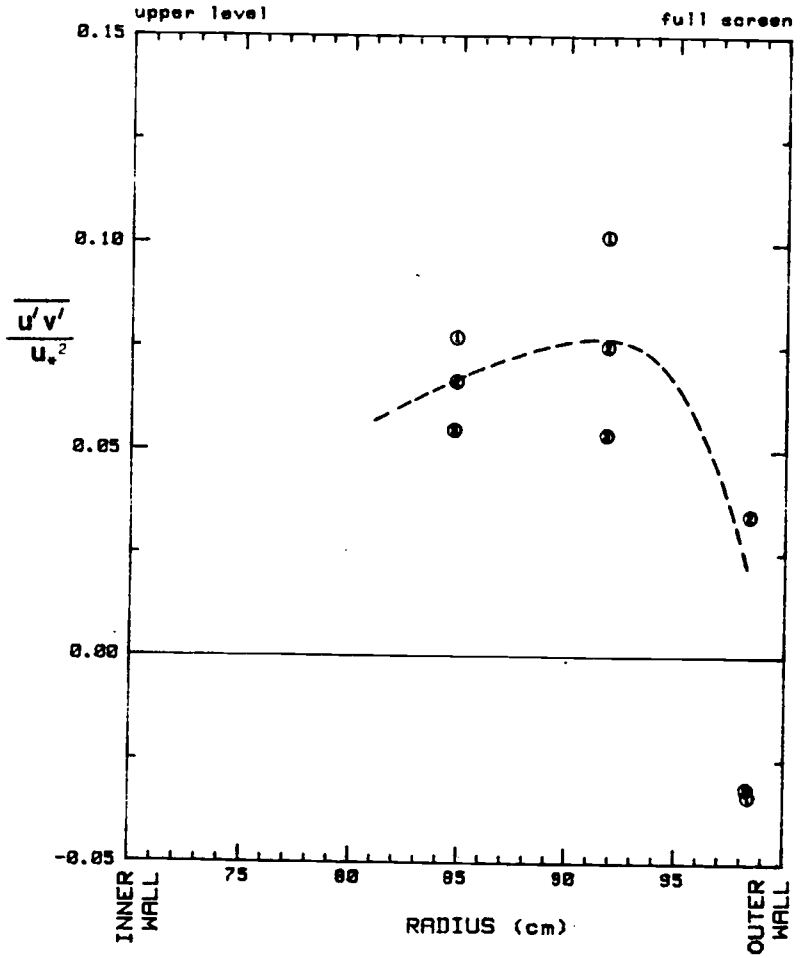

Fig. IV.12. Horizontal profile of $\overline{u'v'}/u_*^2$ at z=0.17h in the full-screen mode.

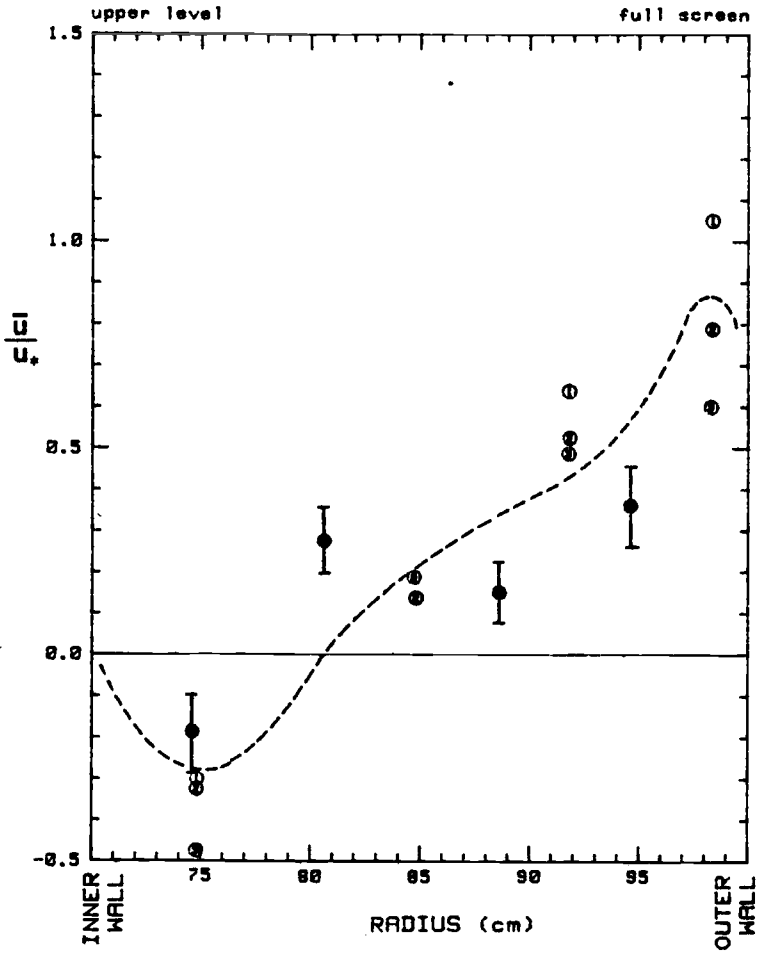

Fig. IV.13. Horizontal profile of $\overline{u}/u_*$ at z=0.17h in the full-screen mode. The dark circles are the averaged particle speeds with their standard deviations (error bars).

The vertical profiles were measured in Exps. 5, 6 and 7 at the center of the annulus area (15 cm from the inner wall). Tables A.5 - A.7 contain the hot-film data, and the results are presented in Figs. IV.14a - IV.18a. The vertical profile of $\overline{v}$ shown in Fig. IV.14a suggests that the flow is well mixed vertically throughout most of the mixed layer. Its magnitude decreases with time due to the effects of side wall drag, which is proportional to the mixed-layer depth. It can also be seen that a substantial amount of the momentum is transported to the denser lower layer, probably by molecular friction and also detrainment of the mixed-layer fluid into the lower layer. The decrease of the mean velocity jump $\Delta\overline{v}$ across the interface with time suggests that the intensity of the locally generated turbulence would decrease with time consequently. This effect can be seen in Figs. IV.15a and IV.16a where the small peak of the turbulent intensities exists near the interface ($z/h \simeq 1$), and its magnitude decreases with time (from ① to ② in Figs. IV.15a and IV.16a). These figures also show that the intensities of the turbulence above the level $z=0.2h$, which corresponds to $z=0.4u_* \overline{r}/\overline{v}$, are much larger than those below.

The vertical profile of $\overline{v'w'}$ given in Fig. IV.17a shows that the surface stress does not extend to the layer

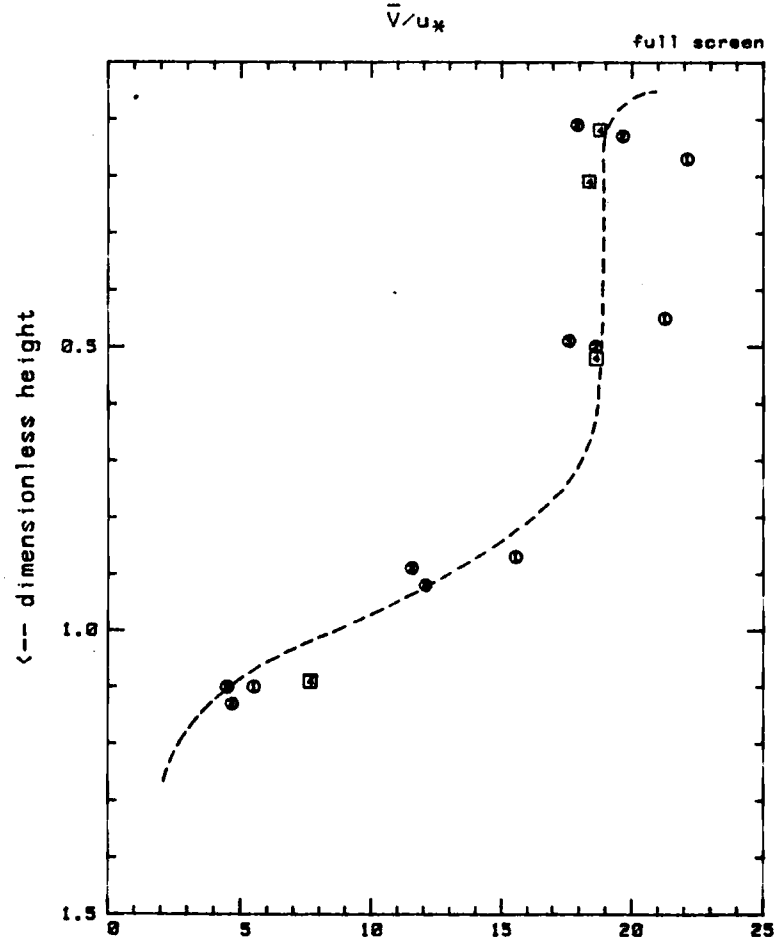

Fig. IV.14a. Vertical profile of $\overline{v}/u_*$ at r=85 cm in the full-screen mode.

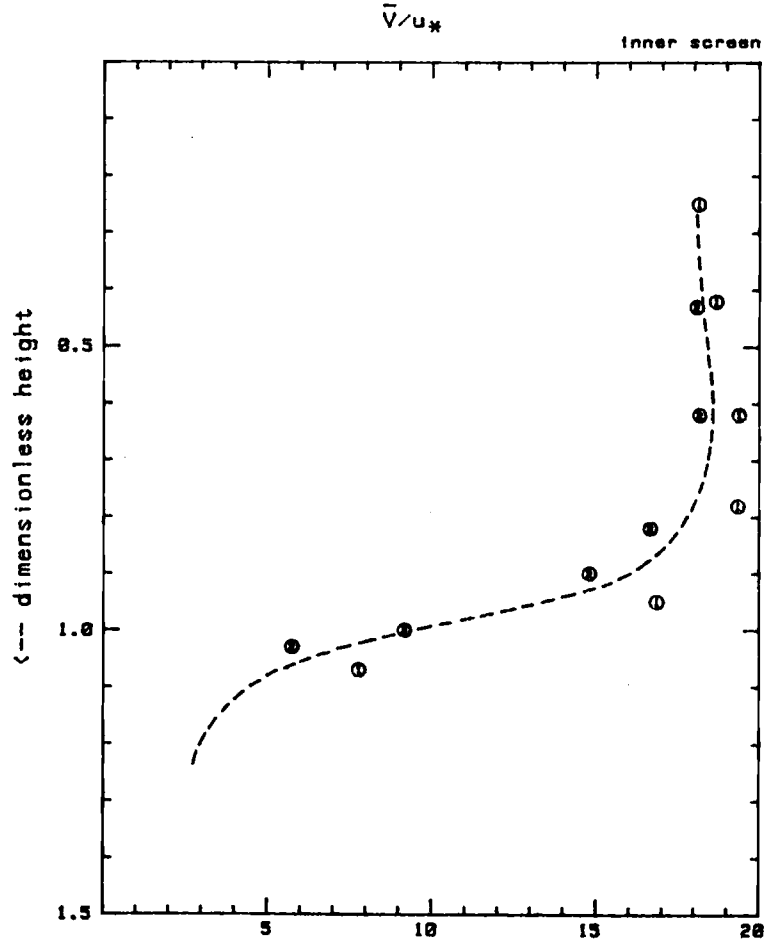

Fig. IV.14b. Vertical profile of $\overline{v}/u_*$ at r=85 cm in the inner-screen mode.

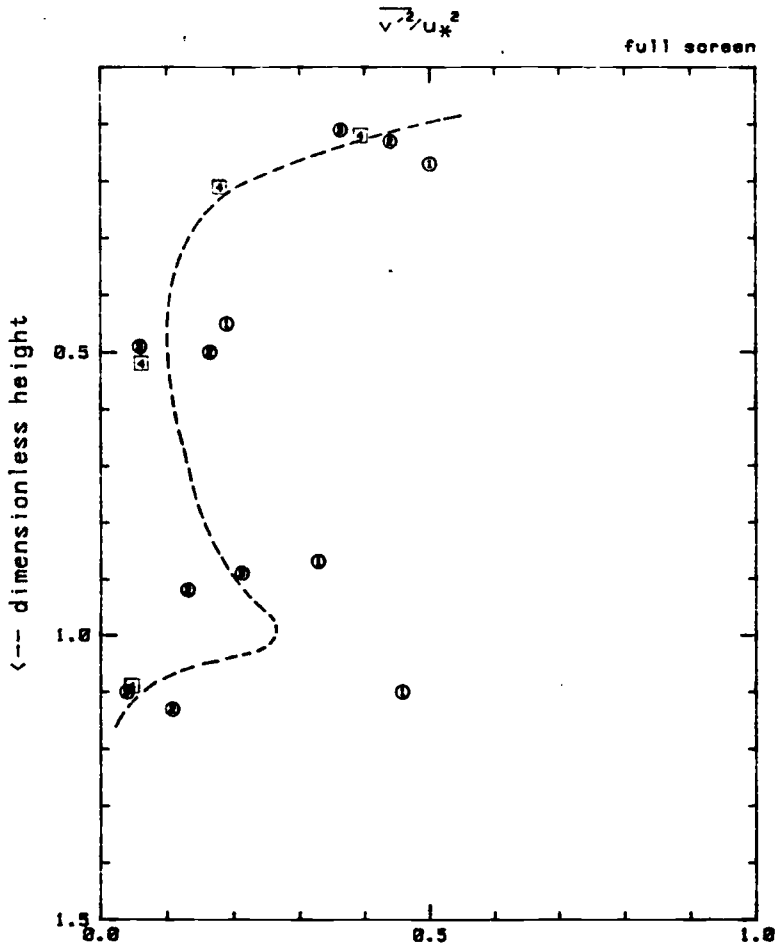

Fig. IV.15a. Vertical profile of $\overline{v'^2}/u_*^2$ at r=85 cm in the full-screen mode.

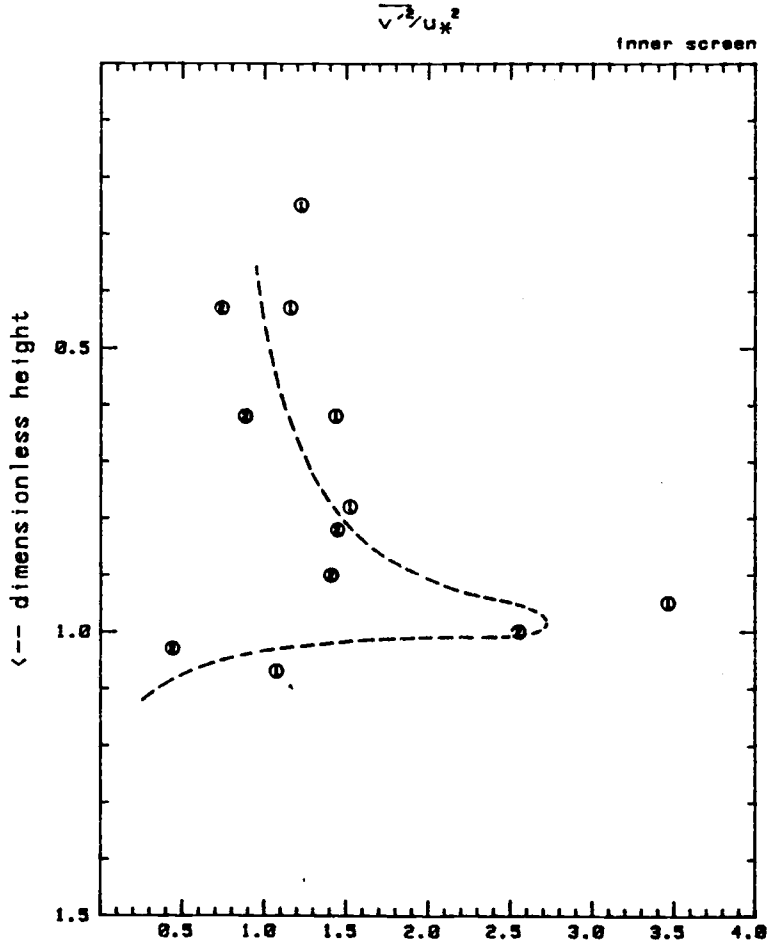

Fig. IV.15b. Vertical profile of $\overline{v'^2}/u_*^2$ at r=85 cm in the inner-screen mode.

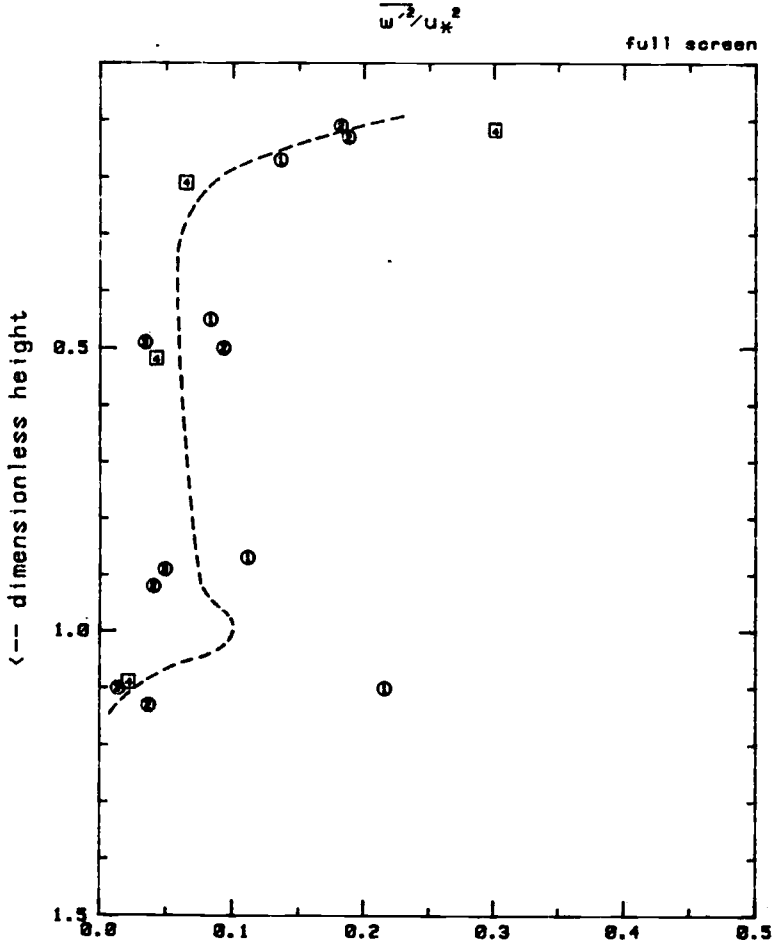

Fig. IV.16a. Vertical profile of $\overline{w'^2}/u_*^2$ at r=85 cm in the full-screen mode.

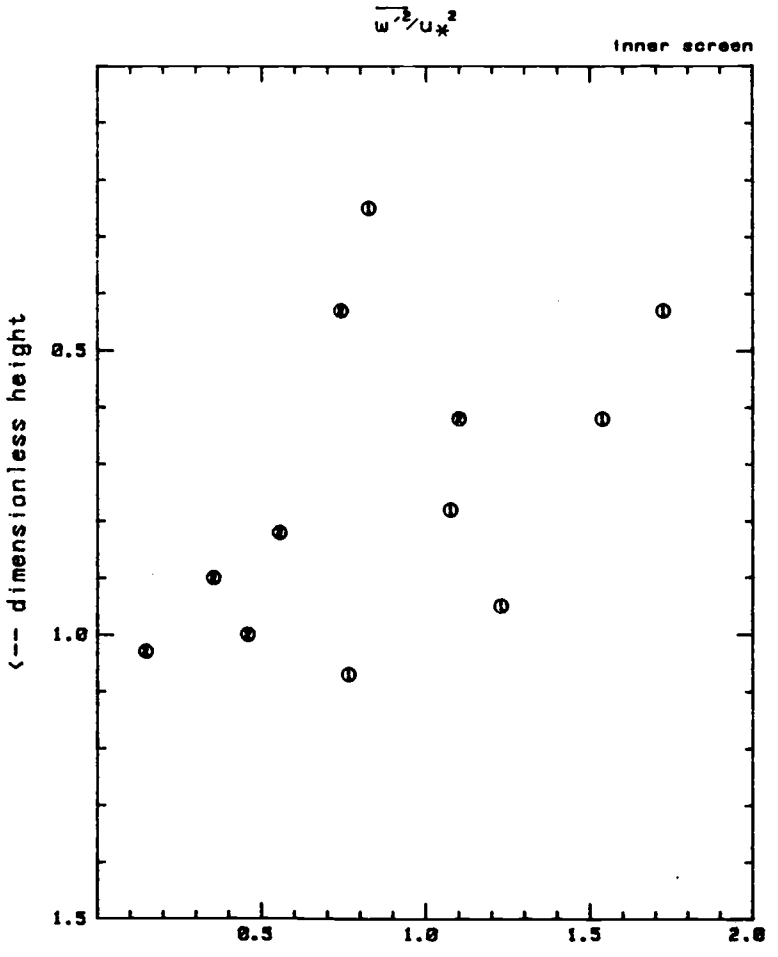

Fig. IV.16b. Vertical profile of $\overline{w'^2}/u_*^2$ at r=85 cm in the inner-screen mode.

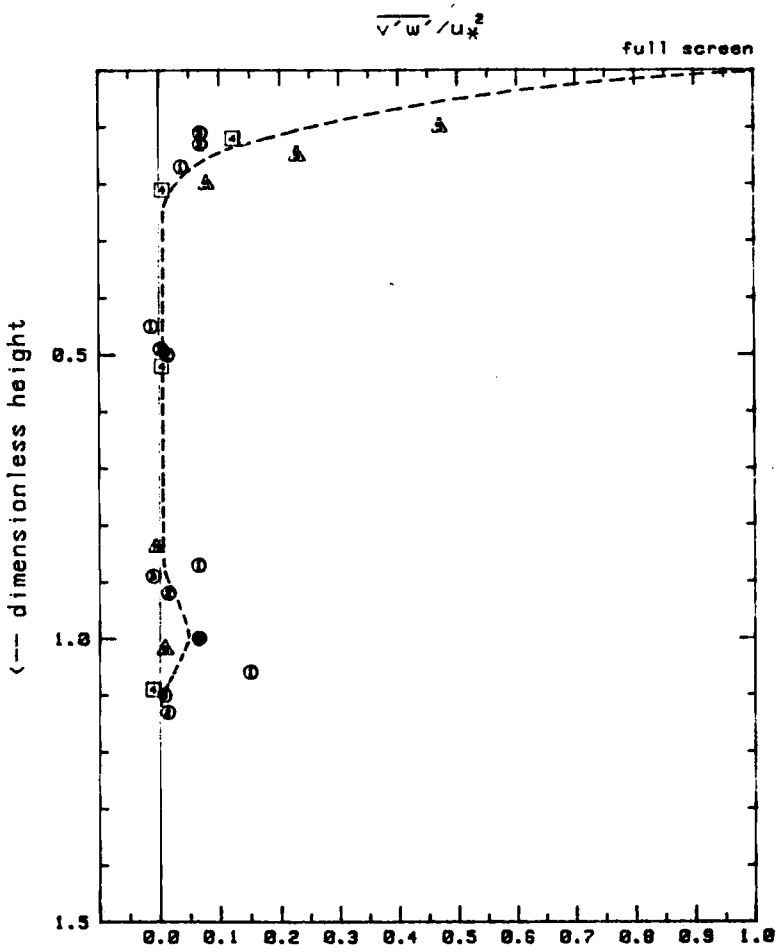

Fig. IV.17a. Vertical profile of $\overline{v'w'}/u_*^2$ at r=85 cm in the full-screen mode. The dark circle is the value of $-\Delta v\ W_e/u_*^2$ at z≈h in Exp. 5.

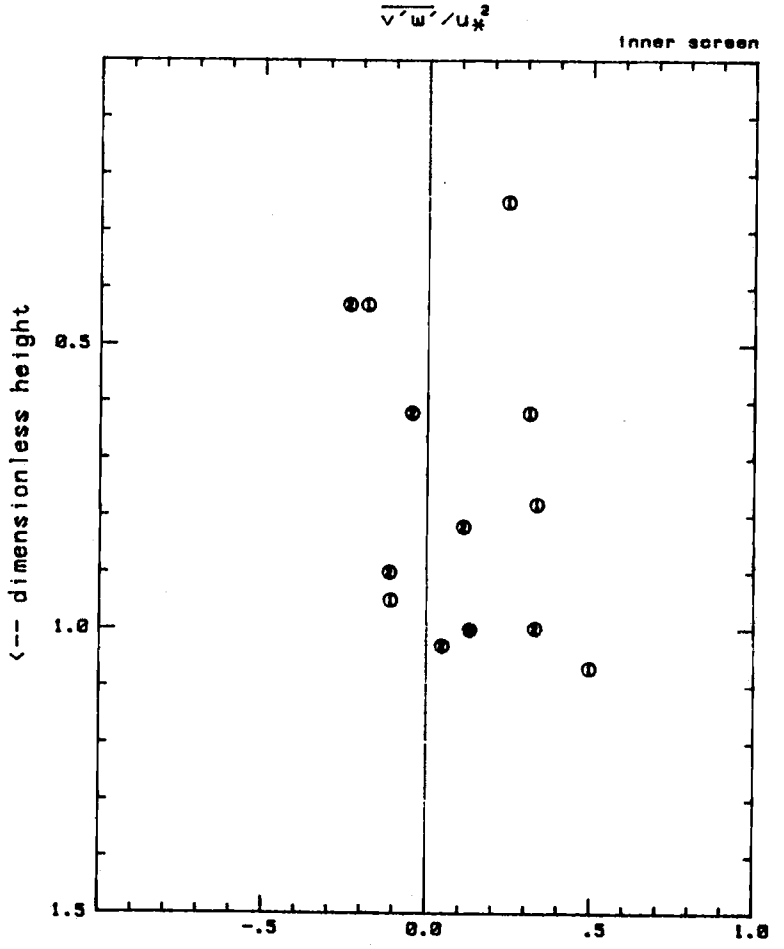

Fig. IV.17b. Vertical profile of $\overline{v'w'}/u_*^2$ at r=85 cm in the inner-screen mode. The dark circle is the value of $-\Delta v\ W_e/u_*^2$ at z≈h in Exp. 11.

below $z = 0.4u_*\bar{r}/\bar{v}$. This finding is very important in the sense that the mixed-layer below this depth (the interior region) is not directly driven by the applied surface stress. The underlying assumption of the mixed layer growth experiment, i.e. mixing by the external surface-stress, therefore does not apply to the annulus experiment when the rotating screen occupies the entire annulus area.

The vertical profiles of the turbulence (Figs. IV.15.a, IV.16a and IV.17a) and the horizontal profiles of the mean velocity components at the upper level (Figs. IV.8 and IV.13) suggest that the layer above $z=0.4u_*\bar{r}/\bar{v}$ is similar to a turbulent Ekman layer in which the pressure gradient, centrifugal and turbulent frictional forces are nearly balanced. The equations of motion in the Ekman layer can be obtained by taking the time average of Eqs (16) and (17) after the Reynolds decomposition of the variables, and then neglecting presumably unimportant terms. These equations become

$$\frac{\partial \bar{u}}{\partial t} = \frac{\bar{v}^2}{r} - \frac{\partial \overline{u'v'}}{\partial z} - \frac{1}{\rho_o}\frac{\partial \bar{p}}{\partial r} \simeq 0, \qquad (21)$$

$$\frac{\partial \bar{v}}{\partial t} = -\frac{\bar{u}\bar{v}}{r} - \frac{\partial \overline{v'w'}}{\partial z} \simeq 0. \qquad (22)$$

The depth of the turbulent Ekman layer in the present work is consistent with the results from the numerical

experiment of Deardorff (1970) and the laboratory experiment of Howroyd and Slawson (1974). They found the layer depth to be $0.4u_*/f$, where f is the Coriolis parameter. If $\overline{v}/r$ is replaced by f in Eqs (21) and (22), the two equations become identical with the Ekman equations in the planetary boundary layer. Then, the Ekman layer depth in the annulus should be

$$0.4\ u_*/f = 0.4\ u_*\ \overline{r}/\ \overline{v} = 0.4(0.8)(85)/18 = 1.5\ (cm)$$

which agrees quite well with the layer depth found in the present work.

The vertical component of the mean velocity, $\overline{w}$, given in Fig. IV.18a shows that there is a weak upward motion with its maximum magnitude in the central region. This result along with the profiles of $\overline{u}$ in Figs. IV.6a and IV.13 suggests that the fluid moves outward in the Ekman layer, comes down along the outer wall, and then spreads horizontally into the interior region with a small upward velocity component. A sketch of the secondary circulation in the vertical cross section is shown in Fig. IV.19. Further reference to this interior region should be understood to represent that portion of the mixed layer after exclusion of the turbulent Ekman layer, the outer-wall layer and the wedge region.

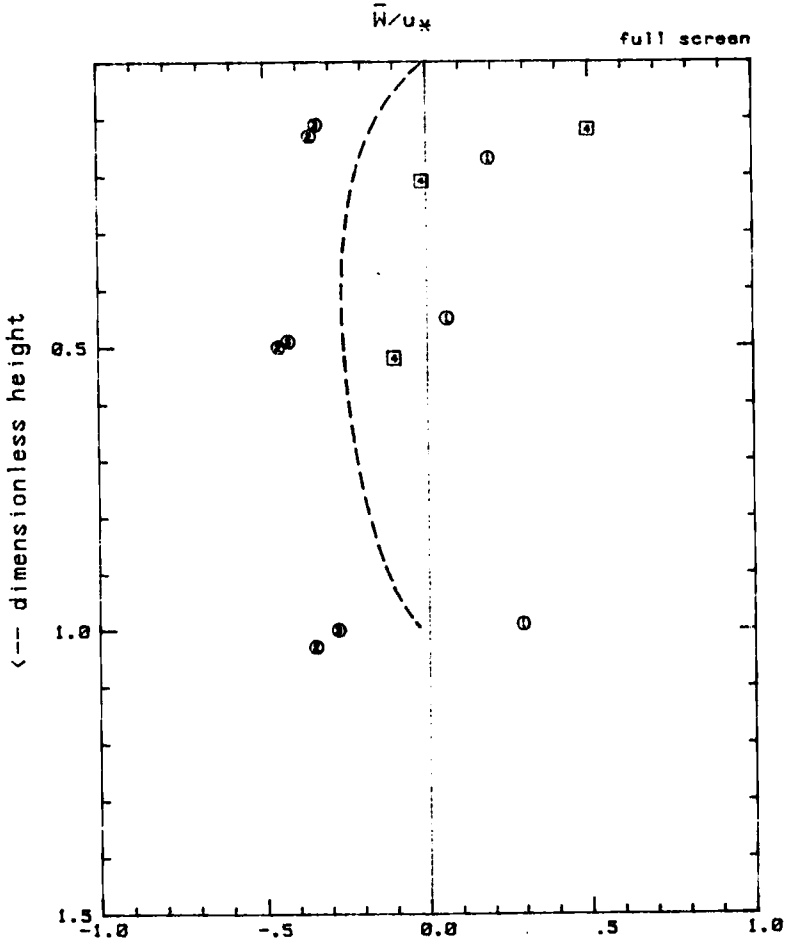

Fig. IV.18a. Vertical profile of $\overline{w}/u_*$ at r=85 cm in the full-screen mode.

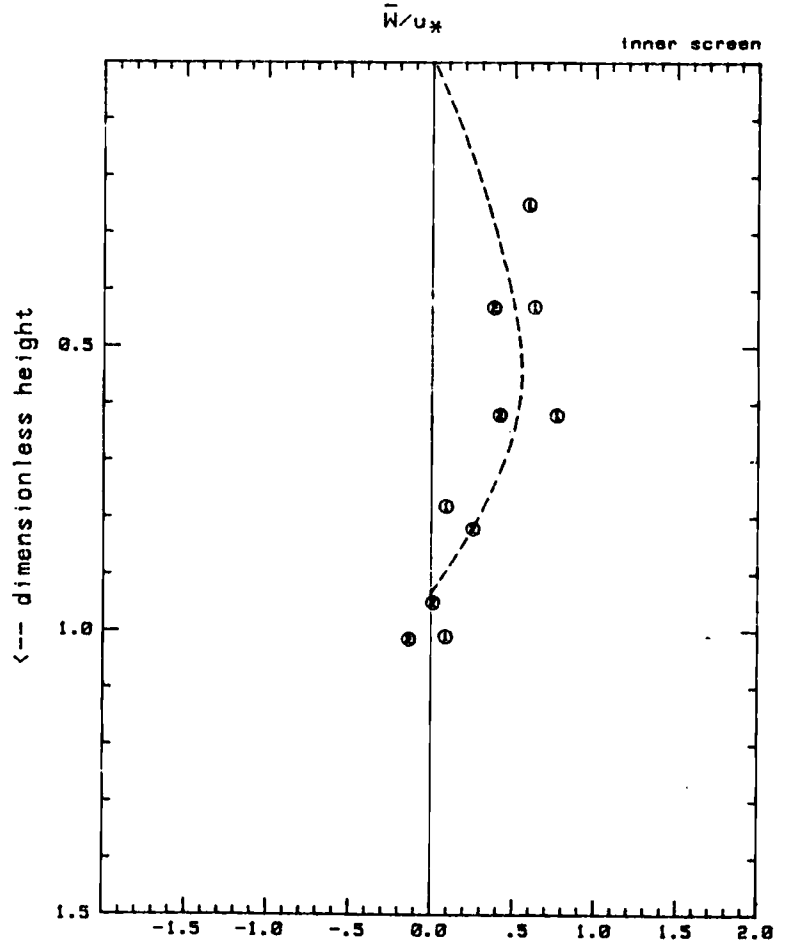

Fig. IV.18b. Vertical profile of $\overline{w}/u_*$ at r=85 cm in the inner-screen mode.

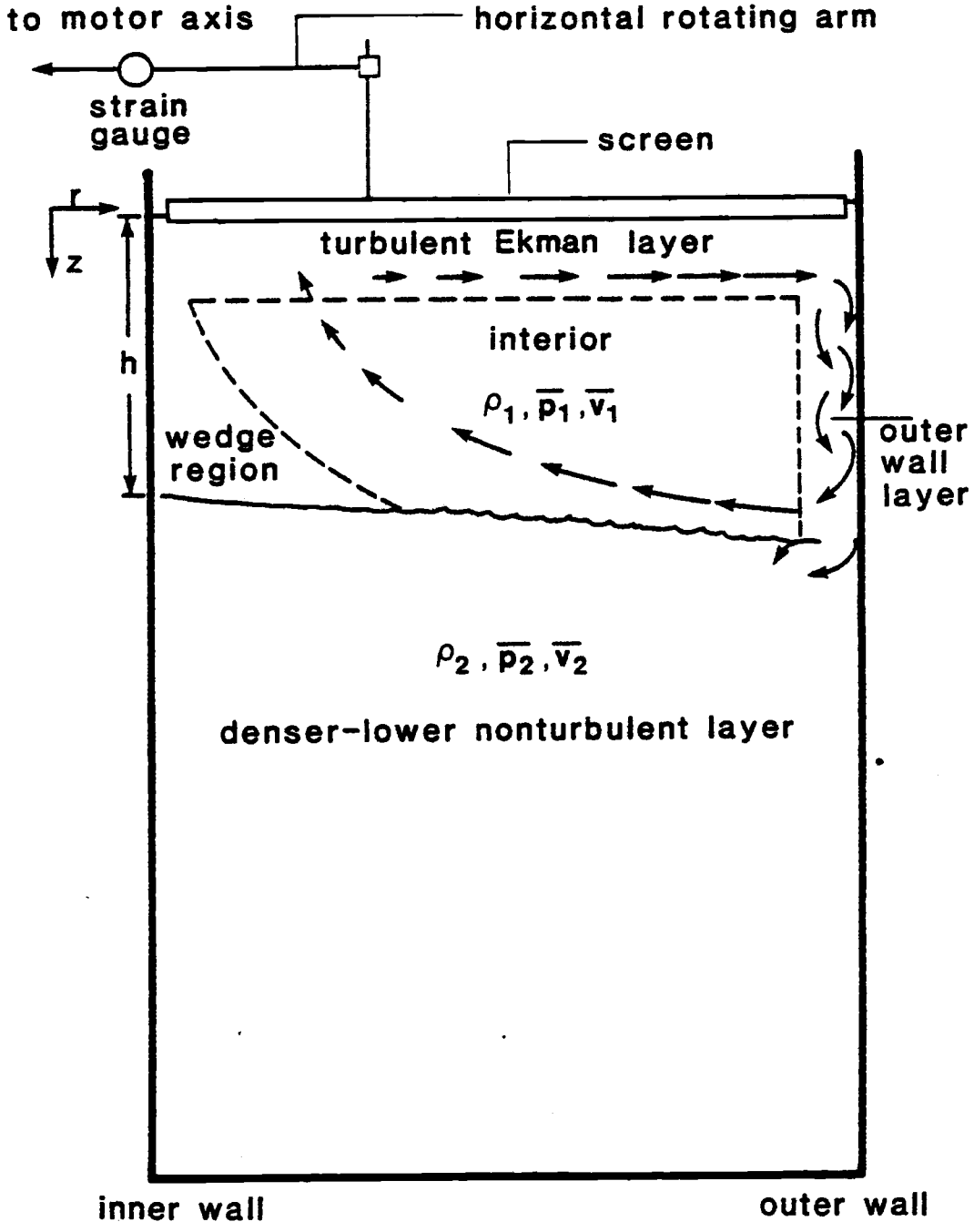

Fig. IV.19. Sketch of the vertical cross-section of the annulus channel and the secondary circulation in the full-screen mode.

IV.3 Flow structure in inner-screen mode

The horizontal profiles of the fluid circulation for the inner-screen mode were measured in Exps. 8, 9 and 10 at z=4 cm. Tables A.8 - A.10 contain the hot-film data, and Figs. IV.1.b - IV.1.b present the results. The horizontal profiles of $\overline{v}$ and the angular momentum given in Figs. IV.1b and IV.2b show that the inertially stable region is confined to half of the region it occupied in the full-screen mode. The horizontal profiles of the turbulent intensities in Figs. IV.3b and IV.4b show that a layer of considerably greater turbulent intensity is no longer prominent near the outer wall. The turbulence is relatively more homogeneous than in the full-screen mode. Its intensities vary by a factor of two instead of by an order of magnitude as in the full-screen mode. The values at the horizontal center closely represent the averages across the annulus area. The entrainment presumably occurs more uniformly across the annulus area.

The radial component, $\overline{u}$, of the mean velocity given in Fig. IV.6b shows that there is a net inward flow in the inner half of the annulus area and a net outward flow in the outer half. This suggests the existence of two separate cells: the inner one in the same direction as the one in the full-screen mode and the outer one in the

opposite direction.

The vertical profiles were measured in Exps. 11 and 12 at the center of the annulus area. Tables A.11 and A.12 contain the hot-film data, and the results are presented in Figs. IV.14b - IV.18b. The mean velocity component $\overline{v}$ is well mixed vertically as shown in Fig. IV.14b. The turbulent intensities in the interior of the mixed layer are an order of magnitude greater than those in the full-screen mode, and the longitudinal component $\overline{v'^2}$ is twice the intensity of the vertical component $\overline{w'^2}$ (Figs. IV.15b and IV.16b).

The Reynolds stress $\overline{v'w'}$ given in Fig. IV.17b is positive on the average, although its values fluctuate very much from the average value. Vertical integration of Eq (22) across the entraining interface by using Leibniz's rule gives $\overline{v'w'} = -\Delta\overline{v}dh/dt$ ($\Delta\overline{v} < 0$) at z=h (see Eq (11) in Mahrt and Lenschow, 1976). The value of $\overline{v'w'}$ computed using this formula agrees quite well with the hot-film measurements (see the dark circle in Fig. IV.17b). This value is somewhat greater than the average value measured in the full-screen mode as shown in Fig. IV.17a. The difference is that the value at the horizonatal center does not represent the horizontal average in the latter mode. The vertical speed given in Fig. IV.18b shows that

there is a weak downward motion at the center of the mixed layer. This is consistent with the $\overline{u}$ profile given in Fig. IV.6b to form the two-cell circulation.

Measurement of the mixed-layer depths near the inner wall and near the outer wall using a horizontally-spread laser beam shows (Table IV.1) that the mixed layer is typically deeper near the outer wall than near the inner wall by about 1 cm. This can be explained as follows. In the interior of the flow (not near the walls), the governing equations, to a first approximation, are

$$\frac{\overline{v}_1^2}{r} = \frac{1}{\rho}\frac{\partial \overline{p}_1}{\partial r} \tag{23}$$

$$\frac{\overline{v}_2^2}{r} = \frac{1}{\rho_2}\frac{\partial \overline{p}_2}{\partial r} \tag{24}$$

$$\frac{\partial \overline{p}_1}{\partial z} = \rho_1 g \tag{25}$$

$$\frac{\partial \overline{p}_2}{\partial z} = \rho_2 g \tag{26}$$

where the subscript "1" denotes the mixed layer, and "2" the denser lower layer (see Fig. IV.19). Vertical integration of Eqs (25) and (26), with the condition $\overline{p}_1(h)=\overline{p}_2(h)$, gives

$$\overline{p}_1(z) = p_s + \rho_1 g(z - h_s) \tag{27}$$

$$\overline{p}_2(z) = p_s - \Delta\rho g h - \rho_1 g h + \rho_2 g z \tag{28}$$

Table IV.1. Data of the mixed-layer depths near the inner wall, h_{in}, and near the outer wall, h_{out}, from Exp. 11.

time (sec)	h_{in} (cm)	h_{out} (cm)
155	5.5	6.2
235	6.3	6.8
280	6.5	7.0
340	7.1	7.8
410	7.8	8.7
460	7.6	9.5
520	8.5	9.4
540	8.8	9.8
635	9.6	10.5
675	10.0	11.1
730	10.2	11.5
760	10.9	11.7
830	11.3	12.5
910	11.8	13.2
940	12.2	13.4
1000	12.7	13.5
1025	12.7	13.6

where $z=h_s(r)$ is the free surface, and p_s is the free surface pressure which is assumed constant. Substituting Eqs (27) and (28) into Eqs (23) and (24), respectively, we get

$$-\frac{\partial h_s}{\partial r} = \frac{\bar{v}_1^2}{rg} \tag{29}$$

$$\frac{\partial h}{\partial r} = \frac{\rho_1 \bar{v}_1^2 - \rho_2 \bar{v}_2^2}{\Delta\rho\, r\, g} \simeq -\frac{\bar{\rho}(\bar{v}_1 + \bar{v}_2)\Delta\bar{v}}{\Delta\rho\, r\, g} \tag{30}$$

where $\bar{\rho} = (\rho_1 + \rho_2)/2$. If $(\bar{v}_1 + \bar{v}_2)/ r$ is replaced by f, Eq (30) is identical with the Margule's formula for the slope of an elevated frontal surface in the atmosphere (see Haltiner and Martin, 1957 page 302). Substituting the typical values: $\bar{v}_1$=15 cm/sec, $\bar{v}_2$=5 cm/sec, $\bar{\rho}$=1.02 gm/cm^3, $\Delta\rho$=0.02 gm/cm^3, $\bar{r}$=85 cm, Δr=20 cm, g=980 cm/sec^2 into Eq (30), we get the result Δh=1.2 cm. This agrees very well with the values measured with the laser beam in the experiment. From this value of Δh we can see that the midxed-layer depths near the inner wall will be 0.6 cm less than the values of h at the center of the annulus. Therefore, the horizontal traverse at z=0.9h for h>7 cm did not penetrate into the lower layer near the inner wall.

IV.4 Entrainment rate

Although the surface stress is not the proper parameter with which to scale the turbulence near the density interface, the overall Richardson number, $R_i = \Delta\rho g h / (\rho u_*^2)$, is used here for purposes of comparison. This overall Richardson number remains constant during an experiment because the value of $\Delta\rho h$ remains constant to maintain the mixed-layer mass budget. Values of the dimensionless entrainment rate ($W_e = (dh/dt) / u_*$) in this work are listed in Table IV.2, and compared with the results of Kantha, Phillips and Azad (1978, referred to as KPA below) and Scranton and Lindberg (1982, referred to as SL below) in Fig. IV.20. For the range of the overall Richardson number 100 to 350, the entrainment rates in the full-screen mode are smaller than KPA's and greater than SL's, while the data in the inner-screen mode are similar to KPA's.

In the full-screen mode it was observed visually that occasional cusps draw the mixed fluid into the denser lower less-turbulent layer. This detrainment introduces some turbulence to the depth several centimeters below the interface. In the later period of an experiment the dimensionless entrainment rate decreased to approximately half of the early period rate. The same phenomenon was

Table IV.2. Entrainment-rate data: $W_e=(dh/dt)/u_*$ is the dimensionless entrainment rate and $R_i=\Delta\rho gh/(\rho u_*^2)$ is the overall Richardson number. The second row of entries of Exps. 1-5 are the entrainment rates of the later periods.

Exp. No.	mode	R_i	W_e	$\Delta\rho$ (gm/cm^3)	u_* (cm/sec)	h_0 (cm)
1	full	236	.0085	.04	.8	4.0
	(after 1100 sec)		.0030			
2	full	200	.0168	.078	1.3	4.0
	(after 400 sec)		.0099			
3	full	236	.0071	.04	.8	4.0
	(after 1000 sec)		.0040			
4	full	236	.0065	.04	.8	4.0
	(after 800 sec)		.0041			
5	full	236	.0064	.04	.8	4.0
	(after 1100 sec)		.0041			
6	full	294	.0031	.04	.8	5.0
7	full	107	.0234	.04	1.3	5.0
8	inner	150	.0600	.02	.8	5.0
9	inner	294	.0078	.04	.8	5.0
10	inner	294	.0097	.04	.8	5.0
11	inner	294	.0110	.04	.8	5.0
12	inner	294	.0135	.04	.8	5.0

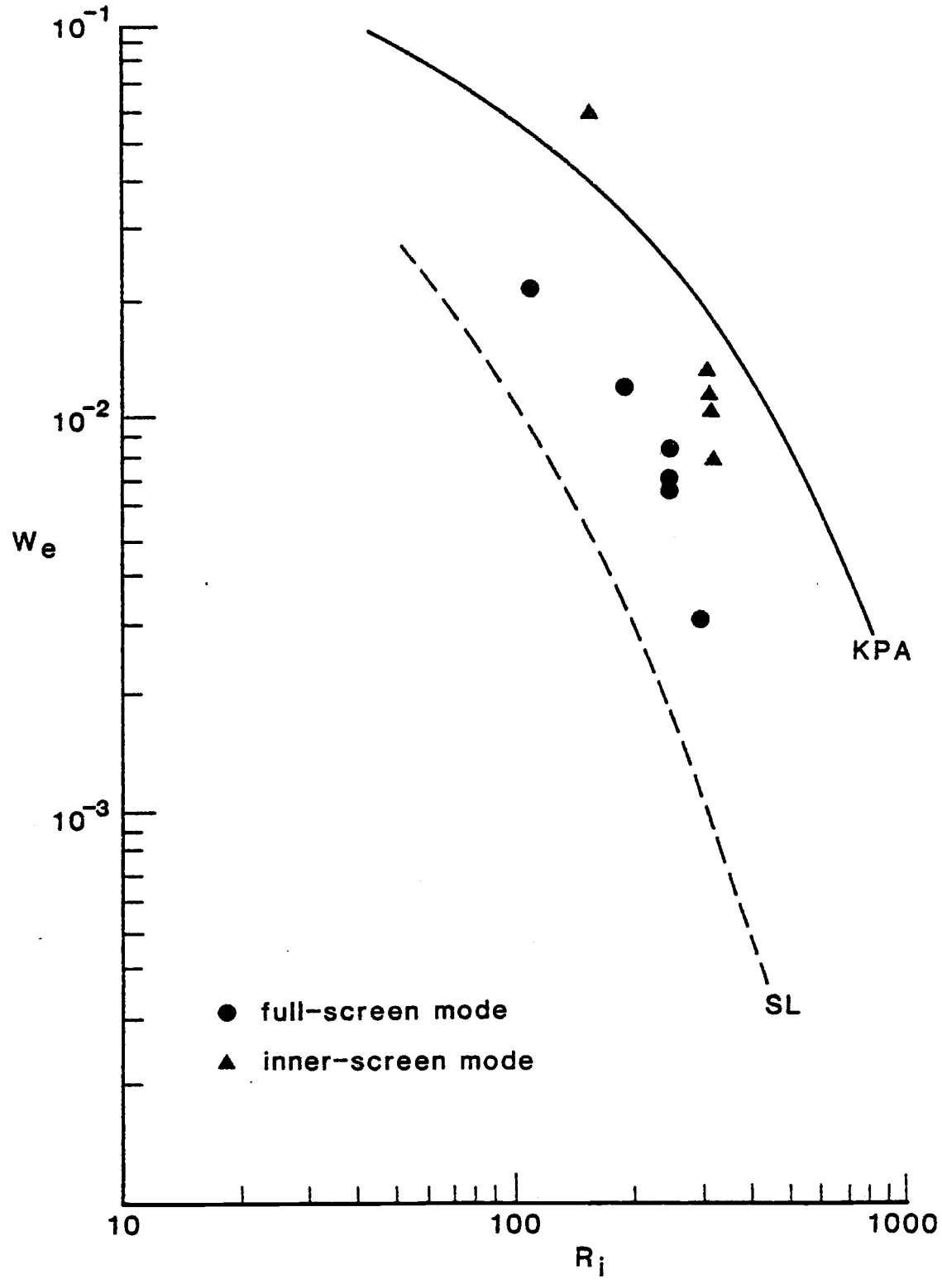

Fig. IV.20. Log-log plot of the dimensionless entrainment rate, $W_e = (dh/dt)/u_*$, versus R_i in comparision with KPA's and SL's data.

observed for an overall Richardson number greater than 300 by Kantha (1975). In the later period, the decrease of the mean velocity shear and the build-up of the wedge region might have reduced the turbulent intensities and the entraining area, respectively, as the entraining interface deepened far away from the surface.

Since the flow in the annulus is so complicated, it is desirable to relate the entrainment rate to the local properties of the turbulence in future rotating-screen annulus experiments. In fact, Turner's (1968) entrainment experiment with an oscillating grid was analyzed with a Richardson number in which the interfacial turbulent length scale and velocity scale, obtained from the hot-film measurements, were used (see Turner, 1973 page 291). The same procedure could be followed in the annulus experiment.

V. CONCLUSIONS AND SUGGESTIONS

When the rotating screen covers the whole annulus area in the mixed-layer growth experiment of the type conducted by KPA, the mixed layer is found to consist of four different regions: the turbulent Ekman layer of depth $0.4u_*\bar{r}/\bar{v}$ just below the rotating screen, the outer-wall layer of considerably much greater turbulent intensities, the wedge region of very slow laminar flow near the inner wall, and the interior region which forms the rest of the mixed layer. The turbulence in the interior region results not from the downward flux of the surface stress but from the outer-wall turbulence advected by the secondary circulation. This advected turbulence is damped out by the inertial stability there. Entrainment is caused mostly by the outer-wall turbulence, partially by the turbulence generated locally by the velocity shear across the density interface, and partially by the outer-wall turbulence advected toward the inner wall by the secondary circulation. Therefore, the entrainment rate is not directly related to the surface stress ρu_*^2.

When the rotating screen is modified to cover the inner 1/4 of the annulus area, the outer-wall layer of considerably greater turbulent intensity is no longer prominent, and the region of inertial stability is

confined to a much smaller area near the inner wall. The turbulent intensities vary horizontally by a factor of two instead of by a factor of ten as in the full-screen mode. Consequently, the entrainment occurs more uniformly across the annulus area than that in the full-screen mode. In these respects, the inner-screen mode is superior to the full-screen mode for mixed-layer growth experiments in an annulus. Although the turbulent intensities vary within a factor of two, the values at the horizontal center of the annulus represent the mean values over the horizontal area in the inner-screen mode. Therefore, turbulence measurement at one point (horizontal center) may suffice for future annulus experiments with the modified screen drive.

Surface contamination of the hot-film probe was unavoidable even though the water used in the experiments was degassed and filtered. This contamination produced a drift of the thermal characteristics of the sensor elements, causing a change in the calibration curve. In order to minimize and to estimate the sensitivity changes caused by the drift, it is recommended that in future experiments the hot-film probe be calibrated in situ before and after an experiment. This could be done by traversing the probe for a limited distance inside the annulus after the towing mechanism is mounted on top of the annulus.

However, the anemometer calibration problems experienced in this study were not so serious as to prevent the preceeding conclusions from being drawn.

REFERENCES

Collis, D.C., and Williams M.J. 1959 Two-dimensional convection from heated wires at low Reynolds numbers. J. Fluid Mech. 6, 357-384.

Comte-Bellot, G., Charnay, G. and Sabot, J. 1981 Hot-wire and hot-film anemometry and conditional measurements. J. of Fluid Mech. 110, 115-128.

Deardorff, J.W. 1970 A three-dimensional numerical investigation of the idealized planetary boundary layer. Geophys. Fluid Dyn. 1, 377-410.

_____, 1981 How time dependence and variable Froude number can explain more rapid entrainment of the two-layer system in annulus experiments. Third Symp. on Turb. Shear Flows, UC Davis, Sept. 9-11, 12.1.

Denman, K.L., and Miyake, M. 1973 Upper layer modification at ocean station PAPA: observation and simulation. J. Phys. Oceanogr. 3, 185-196

Faller, A. J. 1971 Oceanic turbulence and the Langmuir circulations. Annual Rev. of Ecol. & Syst. 2, 201-236.

Haltiner, G.J. and Martin, F.L. 1957 Dynamical and physical meteorology. McGraw-Hill Book Co., Inc.

Howroyd, G.C. and Slawson, P.R. 1975 The characteristics of a laboratory produced turbulent Ekman layer. Boundary-Layer Meteor. 8, 201-219.

Jones, I.S.F. and Mulhearn, P.J., 1982 The influence of external turbulence on sheared interfaces. Submitted to J. Geophys. and Astrophys. Res.

Kantha, L.H. 1975 Turbulent entrainment at the density interface of a two-layer stably stratified fluid system. Tech. Report 75-1, Dept. of Earth and Planetary Sci., Johns Hopkins Universiry.

Kantha, L.H., Phillips, O.M. and Azad, R.S., 1977 On turbulent entrainment at a stable density interface. J. Fluid Mech. 79, 753-768.

Kato, H. and Phillips, O.M., 1969 On the penetration of a turbulent layer into stratified fluid. J. Fluid Mech. 37, 643-655.

Rayleigh, Lord. 1916 On the dynamics of revolving fluids. Scientific Papers. 6, 447-453. Cambridge University Press.

Mahrt, L. and Lenshow, D.H. 1976 Growth dynamics of the convectively mixed layer. J. Atmos. Sci. 33, 41-51.

Niiler, P.P., 1975 Deepening of the wind-mixed layer. J. Mar. Res. 33, 405-422.

Scranton, D.R. and Lindberg, W.R., 1982 An experimental study of entraining stress driven, stratified flow in an annulus. Manuscript, Dept. of Mech. Eng., University of Wyoming, Laramie.

Taylor, G.I., 1923 Stability of a viscous liquid contained between two rotating cylinders. Phil. Trans. Roy. Soc. (London) A. 223, 289-349.

Thermo-Systems Inc. General system information for 1050 series anemometry. 2500 Cleveland Ave. N. St.Paul, Minnesota.

Turner, J.S., 1968 The influence of molecular diffusivity on turbulent entrainment across a density interface. J. of Fluid Mech. 33, 639-656.

_____, 1973 Buoyancy effects in fluids. Cambridge University Press.

Willis, G.E. and Deardorff, J.W. 1974 A laboratory model of the unstable planetary boundary layer. J. Atmos. Sci. 31, 1297-1307.

Zeman, O. and Tennekes, H. 1977 Parametrization of the turbulent energy budget at the top of the daytime atmospheric boundary layer. J. Atmos. Sci. 34, 111-123.

APPENDIX

Table A.1. Hot-film data of Exp. 1: Horizontal traverse in the full-screen mode at z=7 cm, $u_* = 0.8$ cm/sec, $h_0 = 4.0$ cm, $\Delta\rho = 0.04$ gm/cm^3. *'s are plotted in Figs. IV.1a-IV.6a with the encircled numbers "1" and "2".

time (sec)	h (cm)	r-70 (cm)	$\bar{v}$ (cm/sec)	$\bar{u}$ (cm/sec)	$\overline{u'u'}$	$\overline{v'v'}$ (cm/sec)**2	$\overline{u'v'}$	
475.90	6.33	27.14	9.59	-.17	.6991	1.7227	-.5451	
501.15	6.56	28.94	10.79	-.49	.9513	2.4634	-.2833	
523.75	6.79	27.04	11.11	-.97	1.2108	1.6390	-.8391	
551.40	6.84	14.96	4.85	.10	.0481	.3717	.0165	
590.15	7.03	27.04	12.79	-1.41	.5802	1.0042	-.1181	
616.40	7.22	29.01	12.74	-.31	.5442	1.3249	.0189	*
637.70	7.35	26.96	12.99	-1.03	.6493	.5456	-.1101	*
666.10	7.53	14.97	7.65	.15	.0609	.3164	-.0518	*
689.00	7.64	27.17	13.18	-.69	.2964	.6612	-.0661	
711.90	7.87	28.86	12.65	-.28	.4017	.6860	.0225	
736.50	7.86	27.18	13.22	-.64	.2024	.4755	-.0847	
768.20	7.91	15.14	9.00	.03	.0519	.4459	-.0480	
793.65	8.21	27.09	13.09	-.50	.1974	.2571	-.0473	
817.55	8.32	29.00	12.61	-.25	.3758	.5616	.0427	*
844.55	8.32	27.05	12.70	-.37	.1549	.2942	-.0666	*
872.15	8.45	15.00	9.88	-.06	.0565	.1087	-.0243	*
906.40	8.89	27.06	12.57	-.34	.1565	.2271	-.0570	
929.10	8.96	28.84	12.56	-.26	.2473	.4056	-.0304	
955.00	9.23	27.01	12.17	-.22	.1210	.2498	-.0781	
985.25	9.18	14.98	10.36	-.21	.1064	.1101	-.0563	
1011.00	9.31	27.05	12.13	-.20	.0937	.1572	-.0355	
1042.70	9.31	28.91	12.22	-.25	.3734	.5792	-.0526	
1074.55	9.31	26.94	11.59	-.19	.0677	.1451	-.0253	
1103.75	9.60	15.08	10.79	-.20	.0286	.0368	-.0049	
1137.10	9.71	27.09	11.42	-.10	.0898	.1939	-.0610	
1163.70	9.83	28.90	11.92	-.19	.2280	.2952	-.0944	
1199.50	10.16	26.92	10.84	-.01	.0674	.0993	-.0217	
1230.25	10.27	15.00	10.52	-.19	.0389	.0456	-.0097	
1259.15	10.48	26.93	10.70	.01	.0721	.1515	-.0338	
1283.20	10.50	28.83	11.49	-.15	.2222	.2996	-.0756	
1314.80	10.64	26.91	10.45	0.00	.0610	.1062	-.0132	
1348.85	10.74	14.96	10.32	-.13	.0312	.0415	-.0137	
1383.40	10.84	26.92	10.21	.04	.0677	.0778	-.0343	
1408.95	10.74	28.79	11.50	-.29	.1558	.3256	-.1066	
1462.70	10.98	26.95	9.86	-.09	.0518	.0939	-.0386	
1494.85	11.04	14.98	9.88	-.26	.0565	.0278	-.0067	
1534.45	11.21	27.13	10.06	-.10	.0630	.0951	-.0292	
1563.10	11.22	28.91	11.21	-.28	.1659	.2804	-.0884	
1594.80	11.22	27.10	9.99	-.12	.0576	.1073	-.0330	
1617.05	11.22	15.08	9.84	-.22	.0276	.0316	-.0067	

Table A.2. Hot-film data of Exp. 2: Horizontal traverse in the full-screen mode at z=7 cm, u_*=1.3 cm/sec, h_o=5.0 cm, $\Delta\rho$=0.077 gm/cm^3. *'s are plotted in Figs. IV.1a-IV.6a with the encircled number "3".

time (sec)	h (cm)	r-70 (cm)	$\overline{v}$ (cm/sec)	$\overline{u}$ (cm/sec)	$\overline{u'u'}$	$\overline{v'v'}$ (cm/sec)**2	$\overline{u'v'}$	
211.80	6.30	29.36	16.44	-1.16	1.2789	3.9124	-.0669	*
247.65	7.27	27.20	19.38	-3.03	1.2978	2.5536	-.7207	*
277.45	7.65	22.25	15.75	-1.97	.4377	.8733	-.3149	*
307.25	8.70	15.02	13.25	-1.57	.0931	.2103	-.0993	*
340.75	9.05	5.37	7.73	-.98	.0262	.1556	-.0299	*
371.75	9.50	15.07	13.97	-2.15	.0788	.1467	-.0572	
395.85	10.20	22.46	14.81	-2.59	.3070	.4200	-.1383	
424.90	10.50	27.24	16.35	-2.47	.0798	.2416	-.0481	
454.00	11.10	29.38	16.29	-2.41	.3997	.7222	-.2756	
479.20	11.60	27.22	15.30	-2.61	.0902	.2431	-.0944	
513.80	12.00	22.40	13.40	-2.49	.1450	.2371	-.0931	
544.70	12.30	15.01	12.62	-2.49	.0826	.1074	-.0238	
603.30	13.00	5.42	9.37	-1.58	.0599	.1508	-.0302	
660.40	14.20	15.09	12.40	-2.10	.1266	.1394	-.0067	
692.50	14.50	22.36	12.47	-2.10	.0856	.1353	-.0240	
721.40	15.10	27.22	13.43	-2.25	.0879	.2628	-.0927	
747.45	15.80	29.41	14.09	-2.45	.3057	.4771	-.2263	

Table A.3. Hot-film data of Exp. 3: Horizontal traverse in the full-screen mode at z=1 cm, u_*=0.8 cm/sec, h_Q=4.0 cm, $\Delta\rho$=0.04 gm/cm^3. *'s are plotted in Figs. IV.8-IV.13 with the encircled numbers "1" and "2".

time (sec)	h (cm)	r-70 (cm)	$\overline{v}$ (cm/sec)	$\overline{u}$ (cm/sec)	$\overline{u'u'}$	$\overline{v'v'}$ (cm/sec)**2	$\overline{u'v'}$	
107.60	4.18	5.29	4.56	-.42	.0439	.3917	.0203	
133.70	3.96	15.24	9.82	.30	.1748	.2607	.0694	
159.90	4.24	22.29	10.87	.62	.1102	.1727	.0383	
193.70	4.33	28.77	11.79	.75	.3534	.5228	.0752	
220.45	4.73	22.23	11.70	.62	.1529	.1805	.0763	
246.35	4.87	15.21	12.61	.37	.1572	.2028	.0514	
272.35	4.91	5.25	11.55	-.02	.2086	.7824	.0450	
313.90	5.43	15.25	13.31	.35	.2737	.2370	.0520	
339.85	5.48	22.21	12.92	.52	.2201	.3013	.0437	
373.60	5.67	28.76	13.50	.84	.3966	.4879	-.0215	*
395.75	5.78	22.19	12.79	.51	.2185	.2712	.0650	*
432.30	6.02	15.20	13.15	.11	.2277	.1837	.0494	*
463.30	6.40	5.23	12.40	-.24	.1562	.5162	-.0268	*
490.50	6.31	15.29	12.77	.18	.2458	.2805	.0253	
519.50	6.36	22.23	12.12	.43	.2411	.2130	.0681	
548.00	6.46	28.75	12.60	.63	.2304	.3954	.0220	*
593.85	6.62	22.21	12.08	.42	.2480	.2512	.0480	*
620.10	6.80	15.20	12.33	.11	.2030	.1655	.0426	*
647.60	7.10	5.21	11.36	-.26	.1028	.6968	-.0163	*
677.95	7.28	15.22	12.15	.15	.2333	.2369	.0487	
708.15	7.20	22.25	11.57	.37	.2112	.1977	-.0215	
736.15	7.44	28.74	11.78	.43	.2812	.2868	.0054	
771.50	7.36	22.23	11.36	.26	.2027	.2218	-.0152	
797.40	7.57	15.21	11.60	.06	.1923	.1096	.0276	
822.35	7.89	5.27	11.32	-.42	.1017	.3298	.0091	
853.10	7.90	15.31	11.36	.13	.1265	.1138	.0199	
888.60	8.18	22.25	10.98	.33	.2286	.2674	.0618	
920.20	8.11	28.73	11.44	.32	.2857	.3919	-.0422	
950.85	8.15	22.24	10.86	.11	.1634	.2224	.0275	
973.80	8.12	15.27	10.94	-.15	.1237	.1212	.0142	
1006.85	8.12	5.28	10.78	-.54	.0600	.2707	-.0019	
1041.80	8.57	15.27	10.63	-.08	.0965	.1151	.0263	
1069.95	8.95	22.19	10.03	.04	.1624	.1868	.0106	
1097.30	8.97	28.75	10.31	0.00	.1875	.3269	-.0454	
1128.25	9.03	22.22	10.15	.14	.1656	.2281	.0301	
1158.10	9.08	15.23	10.23	.05	.1036	.0656	.0021	
1182.95	9.31	5.29	10.19	-.54	.0829	.2188	-.0451	
1214.20	9.51	15.24	9.91	-.14	.0945	.0976	.0290	
1243.55	9.54	22.07	9.61	.15	.1629	.1806	.0108	
1268.90	9.48	28.83	10.28	.32	.3094	.4295	-.0253	
1301.40	9.46	22.19	9.79	.25	.1651	.1663	.0009	
1332.25	9.70	15.19	9.76	.03	.0724	.0583	.0133	
1363.45	10.13	5.29	9.83	-.55	.0328	.0930	.0082	

Table A.4. Hot-film data of Exp. 4: Horizontal traverse in the full-screen mode at z=1 cm, u_*=0.8 cm/sec, h_0=4.0 cm, $\Delta\rho$=0.04 gm/cm^3. *'s are plotted in Figs. IV.8-IV.13 with the encircled number "3".

time (sec)	h (cm)	r-70 (cm)	$\overline{v}$ (cm/sec)	$\overline{u}$ (cm/sec)	$\overline{u'u'}$	$\overline{v'v'}$ (cm/sec)**2	$\overline{u'v'}$	
212.00	4.46	5.17	10.20	-.35	.2532	.7556	.0577	
242.95	4.47	15.20	12.65	-.12	.1778	.2542	.0258	
273.30	4.63	22.15	12.30	.49	.1990	.2508	.0529	
304.85	4.84	28.71	13.03	.34	.1638	.1583	.0466	
338.95	5.03	22.17	13.23	.44	.2526	.3838	.0227	
364.25	5.15	15.14	13.92	.08	.2662	.1536	.0284	
395.50	5.33	5.14	13.27	-.45	.2371	.9174	-.1132	
504.25	5.80	5.19	13.35	-.38	.1757	.5758	-.0105	*
541.05	5.98	15.11	13.69	.15	.2658	.1665	.0351	*
568.15	6.16	22.17	13.28	.39	.2083	.2853	.0344	*
602.40	6.15	28.68	13.79	.48	.3012	.3657	-.0203	*
629.35	6.33	22.06	13.41	.17	.2309	.2093	.0799	
658.65	6.52	15.09	13.73	-.07	.2103	.0908	.0052	
690.75	6.67	5.11	12.81	-.38	.1291	.8901	-.0839	
722.00	6.97	15.19	13.35	.13	.2463	.1906	.0393	
752.15	6.89	22.21	12.85	.37	.2267	.2991	.0586	
784.05	6.93	28.60	13.14	.55	.3565	.3060	-.0276	
821.40	7.00	22.14	13.01	.35	.3394	.2450	.0584	
846.65	7.26	15.09	13.08	-.08	.1676	.1559	.0488	
880.20	7.55	5.14	12.36	-.47	.1037	.5534	-.0234	
906.75	7.65	15.13	12.60	.02	.1299	.1223	.0276	
936.50	7.62	22.19	11.94	.21	.1522	.1658	.0434	
968.75	7.69	28.68	11.85	.36	.1881	.2518	.0064	
1012.90	7.79	22.13	11.84	.30	.2203	.2185	-.0104	
1041.80	7.99	15.16	11.96	-.07	.0971	.0662	.0182	
1072.70	8.09	5.17	11.99	-.40	.0899	.2011	-.0267	
1111.95	8.43	15.17	11.72	.09	.0859	.0815	.0218	
1143.40	8.27	22.16	11.16	.20	.1349	.1813	.0239	
1178.20	8.33	28.71	11.44	.35	.1788	.3290	.0323	
1219.55	8.39	22.13	11.04	.19	.1751	.2386	.0088	
1248.40	8.61	15.19	11.35	-.06	.0892	.0790	.0062	
1283.70	9.00	5.17	11.09	-.51	.1055	.3456	.0071	
1311.55	9.17	15.13	10.84	-.16	.0739	.0712	.0165	
1339.35	8.97	22.15	10.54	.05	.1524	.2470	.0080	
1372.00	9.08	28.73	10.73	.08	.2417	.3454	-.0372	
1402.40	9.12	22.09	10.44	-.08	.1487	.2642	.0144	
1428.20	9.07	15.18	10.59	-.20	.0823	.0927	.0071	
1459.80	9.40	5.19	10.68	-.57	.0490	.0840	-.0127	

Table A.5. Hot-film data of Exp. 5: Vertical traverse in the full-screen mode at r=85 cm, u_*=0.8 cm/sec, h_0=4.0 cm, $\Delta\rho$=0.04 gm/cm^3. *'s are plotted in Figs. IV.14a-IV.18a with the encircled numbers "1", "2" and "3".

time (sec)	h (cm)	z (cm)	$\overline{v}$ (cm/sec)	$\overline{w}$ (cm/sec)	$\overline{v'v'}$	$\overline{w'w'}$ (cm/sec)**2	$\overline{v'w'}$	
290.75	5.23	5.50	9.00	1.97	.2316	.0777	.0410	
324.30	5.35	4.54	15.52	1.13	.4376	.1099	-.0377	
354.60	5.57	2.49	17.96	.07	.1882	.0794	-.0033	
383.50	5.73	.97	17.69	.15	.3188	.0868	.0233	*
417.95	6.20	2.80	17.00	.05	.1210	.0531	-.0087	*
444.90	6.21	5.42	12.42	.94	.2098	.0708	.0408	*
472.10	6.10	6.81	4.38	1.27	.2928	.1382	.0952	*
633.60	6.97	7.73	4.68	.65	.3259	.0695	.0678	
659.20	7.14	7.11	8.93	.82	.2180	.0401	.0056	
685.65	7.47	3.62	15.73	-.35	.1406	.0659	.0108	
715.00	7.65	.94	15.71	-.29	.2810	.1202	.0438	*
749.75	7.81	3.89	14.89	-.37	.1048	.0593	.0083	*
778.20	7.85	7.20	9.65	.31	.0835	.0259	.0087	*
808.20	7.79	8.84	3.73	.21	.0688	.0235	.0080	*
875.20	8.07	8.85	4.36	.57	.0746	.0354	.0184	
909.60	8.25	7.22	11.52	.55	.1531	.0435	.0267	
933.25	8.36	4.10	14.36	-.44	.1003	.0608	.0055	
960.25	8.59	.94	14.33	-.27	.2321	.1164	.0437	*
991.20	8.95	4.38	14.08	-.34	.0375	.0216	.0011	*
1020.00	9.07	8.04	9.22	.39	.1356	.0314	-.0074	*
1049.95	9.03	9.96	3.58	.06	.0252	.0088	.0044	*
1121.90	9.27	8.22	9.78	.65	.1411	.0297	-.0140	
1159.55	9.54	4.69	13.52	-.29	.0650	.0383	.0002	
1186.40	9.69	.96	13.57	-.12	.1381	.0654	.0284	
1212.90	9.83	4.83	13.34	-.33	.0308	.0191	-.0031	
1240.80	10.00	9.53	6.97	.70	.0692	.0632	-.0009	
1269.40	10.09	10.41	3.68	.35	.0748	.0329	.0247	
1299.75	9.98	9.15	8.79	.67	.1923	.0232	.0031	
1331.75	10.13	5.12	13.17	-.12	.0543	.0259	.0012	
1360.35	10.34	.95	13.17	-.01	.1750	.0790	.0418	
1388.65	10.50	5.25	12.66	-.32	.0246	.0219	.0016	
1416.65	10.47	9.47	7.96	.26	.1556	.0222	-.0159	
1450.85	10.53	11.42	3.21	.08	.0387	.0134	.0043	

Table A.6. Hot-film data of Exp. 6: Vertical traverse in the full-screen mode at r=85 cm, u_*=0.8 cm/sec, h_0=5.0 cm, $\Delta\rho$=0.04 gm/cm^3. *'s are plotted in Figs. IV.14a-IV.18a with the squares.

time (sec)	h (cm)	z (cm)	$\overline{v}$ (cm/sec)	$\overline{w}$ (cm/sec)	$\overline{v'v'}$	$\overline{w'w'}$ (cm/sec)**2	$\overline{v'w'}$	
240.50	5.22	.71	13.48	.54	.4209	.3531	.1700	
275.65	5.10	.94	13.80	.24	.4076	.2166	.1530	
297.55	5.31	1.44	14.11	.07	.1505	.0971	.0060	
324.70	5.51	2.44	14.52	-.19	.0683	.0838	-.0185	
368.65	5.84	5.20	11.59	1.19	.1540	.0356	.0132	
418.90	5.72	5.44	10.50	1.05	.1300	.0496	-.0057	
448.10	5.84	3.03	14.77	-.33	.0741	.0556	-.0141	
469.55	5.74	1.75	14.90	-.12	.0434	.0485	-.0048	
491.30	5.65	1.13	14.88	.01	.1764	.0910	.0240	
541.90	6.00	.72	15.22	.38	.3531	.1800	.0991	
557.70	5.96	.72	15.05	.41	.2522	.1927	.0788	*
581.15	5.91	1.23	14.72	-.01	.1149	.0415	.0038	*
603.10	6.01	1.87	14.78	-.13	.0772	.0405	-.0007	*
627.90	6.21	3.25	14.92	-.08	.0397	.0273	.0033	*
655.85	6.37	6.94	6.13	.84	.0303	.0144	-.0073	*
849.35	6.83	6.33	9.93	.75	.0529	.0172	.0056	
883.85	7.02	3.49	14.12	-.08	.0491	.0222	.0029	
909.15	7.07	2.15	13.98	-.02	.0516	.0365	.0050	
941.10	6.96	1.44	14.01	.09	.0600	.0420	.0018	
997.25	7.21	.81	14.07	.43	.2303	.1545	.0744	
1020.80	7.27	1.48	13.67	.06	.0577	.0264	-.0021	
1043.45	7.22	2.33	13.43	-.06	.0403	.0326	-.0011	
1079.35	7.36	3.83	13.51	-.05	.0331	.0166	.0028	
1121.85	7.59	7.07	8.66	.76	.0588	.0350	.0110	
1158.80	7.69	8.66	3.77	.28	.0335	.0066	-.0009	
1183.15	7.74	7.10	9.02	.75	.1186	.0611	.0095	
1206.55	7.89	3.94	13.36	.04	.0334	.0237	-.0007	
1232.35	7.88	2.37	13.38	-.03	.0435	.0245	.0025	
1254.95	7.89	1.55	13.26	.07	.0379	.0326	-.0048	
1286.85	7.91	.84	13.45	.56	.2079	.1089	.0917	
1312.40	8.12	1.66	13.21	.15	.0379	.0272	.0008	
1330.95	8.21	2.52	13.23	.10	.0297	.0230	-.0019	
1351.75	8.19	4.10	13.21	.12	.0391	.0175	.0043	
1380.55	8.14	7.40	8.95	.54	.0880	.0278	.0124	
1430.30	8.37	9.30	3.80	.41	.0274	.0227	-.0138	
1470.90	8.39	7.75	8.90	.61	.1183	.0251	.0034	
1502.25	8.51	4.31	12.76	.46	.0332	.0323	-.0053	

Table A.7. Hot-film data of Exp. 7: Vertical traverse in the full-screen mode at r=85 cm, u_*=1.3 cm/sec, h_0=5.0 cm, $\Delta\rho$=0.04 gm/cm^3. *'s are plotted in Fig. IV.17a with the triangles.

time (sec)	h (cm)	z (cm)	$\bar{v}$ (cm/sec)	$\bar{w}$ (cm/sec)	$\overline{v'v'}$	$\overline{w'w'}$ (cm/sec)**2	$\overline{v'w'}$	
263.75	10.40	1.05	23.67	2.42	2.0777	1.1207	.7958	*
286.25	11.10	1.63	22.74	2.02	1.2699	.5305	.3879	*
316.50	12.01	2.42	21.97	1.81	.4708	.1893	.1338	*
345.40	13.11	10.98	14.61	1.68	.1129	.0276	-.0093	*
370.95	13.70	14.02	6.94	1.68	1.2953	.0416	.0156	*
426.60	15.03	13.51	11.88	1.76	.1020	.0150	.0187	
463.00	15.72	4.82	19.15	1.75	.0529	.0551	.0068	
489.30	15.72	3.47	19.11	1.92	.0881	.0541	.0117	
512.60	15.72	1.76	19.29	2.18	.3766	.2569	.1931	
557.50	15.72	1.11	20.39	3.33	1.5891	1.0679	.8920	

Table A.8. Hot-film data of Exp. 8: Horizontal traverse in the inner-screen mode at z=4 cm, u_*=0.8 cm/sec, h_0=5.0 cm, $\Delta\rho$=0.02 gm/cm^3.

time (sec)	h (cm)	r-70 (cm)	$\bar{v}$ (cm/sec)	$\bar{u}$ (cm/sec)	$\overline{u'u'}$	$\overline{v'v'}$ (cm/sec)**2	$\overline{u'v'}$
101.45	10.00	2.79	9.49	-.34	1.5840	2.8160	-.5264
134.40	11.60	9.90	13.50	-.60	1.1920	1.5270	-.4447
170.85	13.20	19.89	13.87	.61	1.8430	1.7900	.5823
202.10	14.70	27.50	12.60	.20	.6491	.8155	.0996
216.50	15.40	27.49	12.69	.36	.9282	.7104	.1337
254.10	17.00	19.92	13.83	.77	2.1580	1.5180	.4080
286.50	18.60	9.92	12.67	-.25	.7056	.9423	-.1102
326.10	20.00	2.67	10.23	-.15	.1691	.5199	-.0203

Table A.9. Hot-film data of Exp. 9: Horizontal traverse in the inner-screen mode at z=4 cm, u_*=0.8 cm/sec, h_0=5.0 cm, $\Delta\rho$=0.04 gm/cm^3. *'s are plotted in Figs. IV.1b-IV.6b with the encircled number "1".

time (sec)	h (cm)	x-70 (cm)	$\overline{v}$ (cm/sec)	$\overline{u}$ (cm/sec)	$\overline{u'u'}$	$\overline{v'v'}$ (cm/sec)**2	$\overline{u'v'}$	
159.75	6.50	28.17	10.41	.95	1.1570	4.3690	1.0930	
210.55	6.80	20.08	14.34	1.12	2.0330	1.6520	.9706	
249.20	7.00	15.13	17.66	.12	2.4160	3.7920	1.0300	
282.60	7.30	10.08	20.10	-.80	2.9120	2.7950	.2453	
312.75	7.50	5.08	18.44	-.55	1.9360	1.8550	.0050	
337.80	7.60	2.96	15.86	-.44	1.6010	4.8890	-.0265	
378.20	7.80	5.14	18.09	-.57	2.2200	1.8480	-.0401	
403.80	8.00	10.06	20.24	-.42	2.5030	2.5570	.0147	
440.65	8.40	15.18	20.27	.45	2.8440	3.8550	.8766	
471.50	8.70	20.17	18.65	1.31	1.7870	2.0340	.3374	
501.40	8.80	28.23	16.91	1.35	1.0360	2.1100	.1900	
517.60	8.80	28.21	17.33	1.27	.7504	.9961	.0101	*
544.10	8.90	20.13	19.45	1.56	2.2260	2.2300	.6210	*
576.60	9.10	15.10	20.62	.61	1.6810	2.3990	.1476	*
612.20	9.20	10.11	19.49	-.25	.6867	1.0070	.0389	*
636.50	9.20	5.08	18.57	-.53	.7473	1.1640	.0802	*
662.30	9.40	2.75	17.13	-.62	.8283	1.8500	-.2309	
679.85	9.40	2.79	16.89	-.67	.9850	2.1110	-.0953	
711.20	9.70	5.02	18.45	-.64	.8975	1.4110	.2106	
744.90	10.10	10.23	18.00	-.74	.6834	.9603	-.0063	
775.40	10.20	15.13	17.49	.22	1.0750	1.1030	-.2193	
803.00	10.30	20.22	17.71	.45	1.8090	2.1740	.0913	
834.55	10.50	27.95	15.76	.19	.8574	1.0730	-.0538	
849.50	10.50	27.95	15.79	.50	1.0670	1.5830	-.0344	
880.95	10.60	19.80	17.17	.50	1.8580	1.9250	.0634	
906.50	11.00	14.99	17.39	.41	.6988	1.0210	.0882	
946.00	11.10	10.02	17.17	-1.22	.5240	.6664	-.0226	
972.95	11.40	4.92	16.88	-1.10	.7158	.7801	-.0072	

Table A.10. Hot-film data of Exp. 10: Horizontal traverse in the inner-screen mode at z=4 cm, u_*=0.8 cm/sec, h_0=5.0 cm, $\Delta\rho$=0.04 gm/cm^3. *'s are plotted in Figs. IV.1b-IV.6b with the encircled number "2".

time (sec)	h (cm)	r-70 (cm)	$\overline{v}$ (cm/sec)	$\overline{u}$ (cm/sec)	$\overline{u'u'}$	$\overline{v'v'}$ (cm/sec)**2	$\overline{u'v'}$	
219.60	5.68	28.42	11.50	.29	.5564	1.1466	.1945	
257.90	6.44	22.90	13.24	.39	1.5522	1.7724	.5330	
288.10	6.62	18.21	15.79	.32	1.8652	1.6848	.4579	
314.10	7.00	12.86	18.00	-.60	1.9909	2.8661	.3590	
340.55	7.41	8.08	17.95	-1.53	1.2399	2.3942	-.3610	
367.20	7.52	2.90	14.74	-1.26	1.9563	4.2438	-.8582	
415.35	7.88	8.22	17.49	-1.78	1.4387	1.8419	-.0675	
445.70	7.56	13.23	17.69	-.36	1.4087	2.0147	-.3300	
473.55	8.37	18.15	16.71	.20	2.1112	1.6863	.2852	
500.20	8.26	22.85	15.32	.55	1.5753	.7268	.0816	
529.75	8.26	28.49	14.25	.19	.5035	.9696	.1814	*
554.45	8.79	23.00	15.48	.41	1.8846	1.0986	.2531	*
581.95	8.79	17.82	16.86	-.17	1.4132	1.3590	.2944	*
607.00	8.84	13.04	16.40	-.75	.7164	.7011	-.1510	*
630.75	9.22	8.06	15.98	-1.40	.6967	.7173	-.1026	*
655.50	9.58	2.77	14.87	-1.27	.7001	1.2611	-.3804	
695.25	9.60	8.23	15.00	-1.55	.7013	1.0580	-.1870	
722.35	9.96	13.17	15.27	-.59	.5990	1.1600	-.1660	
747.45	10.14	17.98	15.33	-.17	1.0421	1.2227	.1001	
770.10	10.18	22.93	14.49	0.00	1.1714	1.5028	-.0923	
796.25	10.26	28.52	13.84	-.25	.7210	1.0393	-.1766	
819.65	10.37	22.80	15.04	-.04	1.6023	1.2563	.2056	
845.40	10.38	17.80	14.95	-.21	1.0405	1.5002	.2593	
869.35	10.45	13.23	14.52	-.24	.5264	.8707	-.0853	
893.40	10.63	8.07	14.73	-1.41	.5588	.6637	-.0464	
921.75	10.62	2.83	14.12	-1.22	.3966	.4931	-.1151	
937.15	10.77	2.84	13.76	-1.14	.5707	.9456	-.0014	

Table A.11. Hot-film data of Exp. 11: Vertical traverse in the inner-screen mode at r=85 cm, u_*=0.8 cm/sec, h_0=5.0 cm, $\Delta\rho$=0.04 gm/cm^3. *'s are plotted in Figs. IV.14b-IV.18b with the encircled numbers "1" and "2".

time (sec)	h (cm)	z (cm)	$\overline{v}$ (cm/sec)	$\overline{w}$ (cm/sec)	$\overline{v'v'}$	$\overline{w'w'}$ (cm/sec)**2	$\overline{v'w'}$	
132.30	2.09	.77	11.41	1.01	6.0525	1.3964	-.2065	
324.95	3.43	1.68	15.45	1.64	1.5504	1.1413	.0989	
354.85	7.43	4.90	15.15	1.39	1.4536	1.4916	.4280	
403.10	7.59	7.21	14.85	1.32	1.6110	.7462	.3843	
438.10	8.25	8.25	9.55	1.66	4.3301	1.0597	.8136	
467.45	8.48	9.07	6.22	1.00	.6876	.4889	.3165	*
506.45	8.58	8.15	13.47	1.50	2.2142	.7861	-.0716	*
539.10	9.33	7.28	15.47	.70	.9739	.6872	.2136	*
585.25	9.24	5.91	15.50	.61	.9172	.9831	.1986	*
618.20	9.24	4.16	14.94	.50	.7400	1.1029	-.1176	*
650.25	10.12	2.63	14.51	.47	.7820	.5278	.1553	*
686.10	10.56	4.54	14.46	.30	.4713	.4737	-.1533	*
716.25	10.56	6.55	14.53	.33	.5644	.7041	-.0308	*
751.10	11.22	9.20	13.31	.20	.9247	.3548	.0708	*
783.20	11.26	10.13	11.83	1.00	.9016	.2259	-.0730	*
815.95	11.26	11.26	7.33	1.38	1.6321	.2929	.2109	*
844.55	11.89	12.25	4.59	.47	.2797	.0944	.0371	
906.20	12.07	12.07	5.94	1.02	.3058	.2128	.1471	
937.05	12.67	10.90	11.70	.42	.7733	.1849	-.0438	
969.30	12.74	8.54	13.07	-.59	.2627	.2162	.0213	
995.90	13.03	6.12	12.79	-.68	.2545	.2252	.0144	
1020.20	13.16	3.55	12.64	-.14	.3407	.3176	-.0572	

Table A.12. Hot-film data of Exp. 12: Vertical traverse in the inner-screen mode at r=85 cm, u_*=0.8 cm/sec, h_0=5.0 cm, $\Delta\rho$=0.04 gm/cm^3.

time (sec)	h (cm)	z (cm)	$\overline{v}$ (cm/sec)	$\overline{w}$ (cm/sec)	$\overline{v'v'}$	$\overline{w'w'}$ (cm/sec)**2	$\overline{v'w'}$
232.80	5.99	3.07	14.84	1.29	2.2380	1.3067	.2167
266.85	5.92	4.29	15.89	1.21	2.0397	1.5023	.6904
293.80	6.69	5.53	16.05	1.31	2.4705	1.1592	.6022
326.90	6.90	6.88	14.69	1.29	2.0868	.6182	.2600
351.05	7.13	7.87	10.30	1.77	3.5257	1.0246	.5490
380.80	7.50	8.74	6.69	1.07	.9231	.3690	.2600
466.05	7.29	10.22	5.33	.58	.3472	.1670	.0593
503.85	8.31	8.96	12.51	1.68	3.3210	.7558	.1958
531.10	9.04	8.39	15.36	.65	1.2984	.6080	.3335
566.55	9.13	8.27	15.74	.37	1.0643	.6881	.2454
596.95	9.62	6.73	15.77	.49	.8614	.8704	.1695
624.05	9.80	4.93	15.23	.35	.6933	.7435	.1539
656.90	10.06	7.15	14.49	.31	.7219	.5641	.2025
688.45	10.02	9.40	13.76	.36	.9582	.3886	.1150
727.80	10.20	10.18	12.93	.54	1.1153	.2864	.1079
767.70	10.27	11.77	11.76	.54	.8938	.2703	.0669
801.90	10.86	12.89	9.10	1.41	1.8486	.2467	.0047
817.65	10.88	13.06	9.11	1.27	.9939	.1801	.1130
830.50	11.07	13.40	9.34	1.31	.8353	.2054	-.1925
843.35	11.09	13.26	10.01	.98	.6075	.2040	-.0822
874.00	11.32	12.48	10.72	.79	.6813	.3045	.0475
913.90	11.73	11.58	10.95	.58	.5339	.2100	-.0185
944.15	11.90	10.79	11.39	.32	.4891	.1869	-.0018
975.05	11.84	8.34	11.48	.09	.6492	.2042	.0793
1009.40	12.19	6.06	11.29	0.00	.6150	.1907	.0930
1042.30	12.42	8.59	11.28	-.21	1.0538	.2102	-.0218
1055.15	12.50	8.30	11.25	-.19	.6431	.2184	-.0464
1106.40	12.81	8.30	10.89	-.30	.4970	.1924	.0137
1157.65	13.04	8.30	10.74	-.39	.4391	.1938	.0155